geosciences

MDPI

Article

Geochronology, Geochemistry, and Tectonic Implications of the Early Devonian Mafic Intrusions in the Southern Margin of the North China Craton

Kekun Li [1,2], Ruidong Yang [1], Yazhou Fan [3,*], Jianhan Huang [3,*] and Pengyuan Chen [2]

[1] Key Laboratory of Karst Georesources and Environment, College of Resources and Environmental Engineering, Ministry of Education, Guizhou University, Guiyang 550025, China
[2] Henan Geological Bureau, China Chemical Geology and Mine Bureau, Zhengzhou 450011, China
[3] College of Geosciences and Engineering, North China University of Water Resources and Electric Power, Zhengzhou 450046, China
* Correspondence: fanyazhou@ncwu.edu.cn (Y.F.); huangjianhan@ncwu.edu.cn (J.H.); Tel.: +86-0371-65188815 (Y.F.)

Abstract

The Heilongtai–Maogudui (HM) mafic intrusions are exposed in the southern margin of the North China Craton (SNCC), which are contemporaneous with a variety of strategic metal/non-metal minerals (niobium, uranium, and high-purity quartz) and magmatic hydrothermal REE deposits. New geochronology and geochemistry of these intrusions are examined and interpreted to decipher their petrogenesis and tectonic settings. Zircon LA–ICP–MS data formed a concordant cluster, yielding a mean $^{206}Pb/^{238}U$ age of 397.5 ± 3.5 Ma, which is interpreted as an Early Devonian crystallization age. The HM mafic intrusions have similar whole-rock geochemical compositions, containing 48.94–51.51 wt% SiO_2, 1.26–1.61 wt% TiO_2, 5.96–7.13 wt% MgO, and 11.00–12.48 wt% FeO_t. The total alkali contents range from 1.61 wt% to 3.53 wt%, with $Mg^{\#}$ values of 47.23–52.30. The petrographic and geochemical results suggest the fractional crystallization of mainly olivine, clinopyroxene, and minor Fe–Ti oxide in the mafic intrusions. Being of tholeiitic composition, these mafic rocks display relatively flat rare earth element (REE) and trace element patterns, which are similar to those of the normal mid-ocean ridge basalt (N–MORB) and the enriched mid-ocean ridge basalt (E–MORB). The HM mafic intrusions are proposed to originate in the continental extensional environment through 5–10% partial melting of the depleted spinel asthenosphere mantle source. This is attributed to the gravitational delamination of the lithospheric mantle and the upwelling of the hot asthenosphere, marking the end of the Paleozoic Proto–Tethyan orogenic cycle. The Paleozoic strategic mineral deposits are proposed to have formed under this specific tectonic regime.

Keywords: mafic intrusion; extension; Early Devonian; Nanzhao–Fangcheng area; North China Craton

Check for updates

Academic Editors: Maurizio Barbieri and Pujun Wang

Received: 26 April 2026
Revised: 6 June 2026
Accepted: 10 June 2026
Published: 12 June 2026

Copyright: © 2026 by the authors. Licensee MDPI, Basel, Switzerland. This article is an open access article distributed under the terms and conditions of the Creative Commons Attribution (CC BY) license.

1. Introduction

A variety of strategic metal/non-metal minerals (e.g., rare metal, uranium, and high-purity quartz) and magmatic hydrothermal REE deposits are currently recognized in the southern margin of the North China craton (SNCC) and the North Qinling Orogen (Figure 1a). These deposits are mainly associated with pegmatites, carbonate–alkaline intrusions, alkaline granites, and hydrothermal fluid [1–10]. Mineralization occurred in the Mesoproterozoic [10–12],

Neoproterozoic [13], Paleozoic [1–3,8,10], and Mesozoic eras [2,14,15]. Some mantle-derived mafic and intermediate igneous rocks are distributed in the SNCC and the North Qinling Orogen, which are contemporaneous with these deposits [14,16–28]. This suggests that the activity of mantle-derived magmas makes a certain contribution to the ore-forming process, and there is a feasible spatiotemporal relationship between them [14,24–29]. Previous studies have been extensively carried out on the Neoproterozoic and Mesozoic geological processes along the SNCC [17,18,28–31] and the Paleozoic evolution of the North Qinling Orogen [27,32]. However, there is limited information available regarding the Paleozoic evolution of the SNCC [22]. The Paleozoic Heilongtai–Maogudui (HM) mafic intrusions are exposed in the Nanzhao–Fangcheng area (Figure 1a–c) [14,22]. Thus, knowledge and understanding of the genesis and geodynamic setting of these mafic intrusions is crucial in constraining the Paleozoic tectonic evolution of the SNCC and North Qinling Orogen. In this study, new geochronology and geochemistry of the HM mafic intrusions are examined and interpreted to decipher the petrogenesis and tectonic settings. These findings provide new constraints on the sources and the crust–mantle evolution in the study area and contribute to a better understanding of the Paleozoic tectonic evolution and metallogenic framework of the SNCC and North Qinling Orogen.

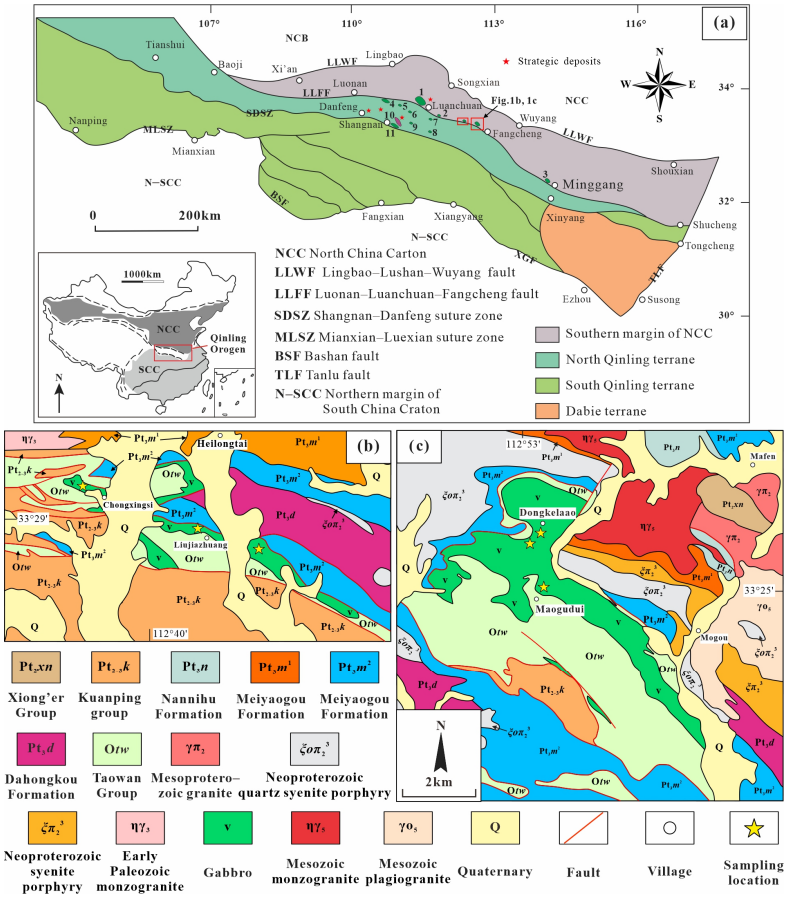


Figure 1. (**a**) Simplified tectonic map of the SNCC and Qinling Orogen (modified from [7,32,33]). (**b**) and (**c**) Schematic geological maps of the HM mafic intrusions in Heilongtai Village and Maogudui Village, respectively (modified from [16,29]). Numbers: 1—Luanchuan gabbro (830 Ma, [18]), 2— Heibian gabbro (119 Ma, [28]), 3—Zhouzhuang gabbro (859 Ma, [17]), 4—Pingdicun appinite (389 Ma, [25]), 5—Erlangping gabbro (464 Ma, [29]), 6—Fanpu diorite (424 Ma, [26]), 7—Erlangping diorite (453 Ma, [24]), 8—Gushanping gabbro (457 Ma, [27]), 9—Zhaigen gabbro (484 Ma, [34]), 10—Songshugou ophiolite (500–493 Ma, [23]), and 11—Fushui mafic complex (488–484 Ma, [20]). The strategic metal/non-metal deposits, represented by the red star symbols, are the Shuimogou REE deposit, Taipingzhen REE deposit, high-purity quartz deposit, and uranium deposit from east to west.

2. Geological Setting

The SNCC is located in the southernmost part of the North China Craton and to the north of the Qinling Orogen, between two main regional thrust faults, i.e., the Lingbao–Lushan–Wuyang fault (LLWF) to the north, and the Luonan–Luanchuan–Fangcheng fault (LLFF) to the south (Figure 1a) [16]. It is an important part of the North China Craton and records the characteristics of the transition from the craton to the orogenic belt [27,32–35]. The LLFF extends in the EW direction, including a series of secondary faults, and each fault develops a compressional fracture zone [26]. The regional strata are involved in compressional deformation zones, e.g., the Kuanping Group in the south, and the Taowan Group, Luanchuan Group, and a segment of the Xiong'er Group in the north [26] (Figure 1a–c). The fault morphology is relatively complex due to the strong superposition of multi-stage structural deformation, which controls the distribution of regional magmatic rocks and mineral deposits [8,16]. A period of intense structural activity occurred in the Devonian between 381 and 371 Ma [36].

The Paleoproterozoic Xiong'er Group is less exposed and is distributed to the north of the HM mafic intrusions (Figure 1c). It mainly consists of volcanic rocks, including basaltic andesite, andesite, rhyolitic lava, and minor pyroclastic rocks [37]. The Neoproterozoic Luanchuan Group is mainly composed of sandstone, marble, schist, phyllite, and alkaline volcanic rocks [16,38,39]. It can be subdivided into four formations: the Sanchuan Formation, the Nannihu Formation, the Meiyaogou Formation, and the Dahongkou Formation [18,38–40] (Figure 1b,c). The Taowan Group is Ordovician in age and is separated by two angular unconformities from the Cambrian and Permian [27]. It mainly consists of phyllite and carbonaceous slate. The complex deformation is thought to result from both the sinistral transpression of the LLFF to the south [27] and south-directed thrusting and folding [36,41]. The Kuanping Group is the northernmost unit in the North Qinling Orogen and is mainly composed of meta-mafic rocks, deformed mica schist, quartzite, marble, and amphibolite [27,32,42]. Magmatic activity is highly developed, featuring Mesoproterozoic granite porphyry, Neoproterozoic syenite porphyry, Paleozoic monzogranite and mafic rocks, and Mesozoic monzogranite and plagiogranite [16] (Figure 1b,c).

3. Petrological Characteristics

The HM mafic rocks are located to the north of the LLFF and are distributed in the Heilongtai area of Nanzhao County and the Maogudui area of Fangcheng County (Figure 1b,c). Generally, these rocks have undergone regional metamorphism from greenschist to low-amphibolite facies, and to a certain extent, they exhibit alteration phenomena such as secondary amphibolization and chloritization. However, the structures of the original mafic rocks are clearly preserved [22] (Figure 2a–f).

The mafic rocks in the Heilongtai area (Sample No. 25NZ–8–1~6) are mainly composed of amphibole (55–75%), plagioclase (15–35%), epidote (1–5%), titanite (1–5%), and a small amount of quartz (Figure 2b,d). Microfibrillar amphibole mostly orients along the long axis, and a few pyroxene crystals retain a pseudomorphism. Plagioclase occurs in an irregular fine-plate columnar shape and is distributed among the amphibole grains. Fine-grained epidote is aggregated and distributed between the amphibole and plagioclase (Figure 2d). The mafic rocks in the Maogudui area (Sample No. 25FC–8–1~3) have a variable medium-grained and relict gabbroic texture and massive structure (Figure 2a,c). They consist of amphibole (50–70%), plagioclase (25–45%), ilmenite (5–10%), and a small amount of chlorite and epidote. Amphibole appears as semi-euhedral long columnar or fibrous aggregates with light green–green polychroism. Plagioclase is granular with a first-order gray interference color, and ilmenite exists as irregular coarse-grained aggregates (Figure 2e,f).

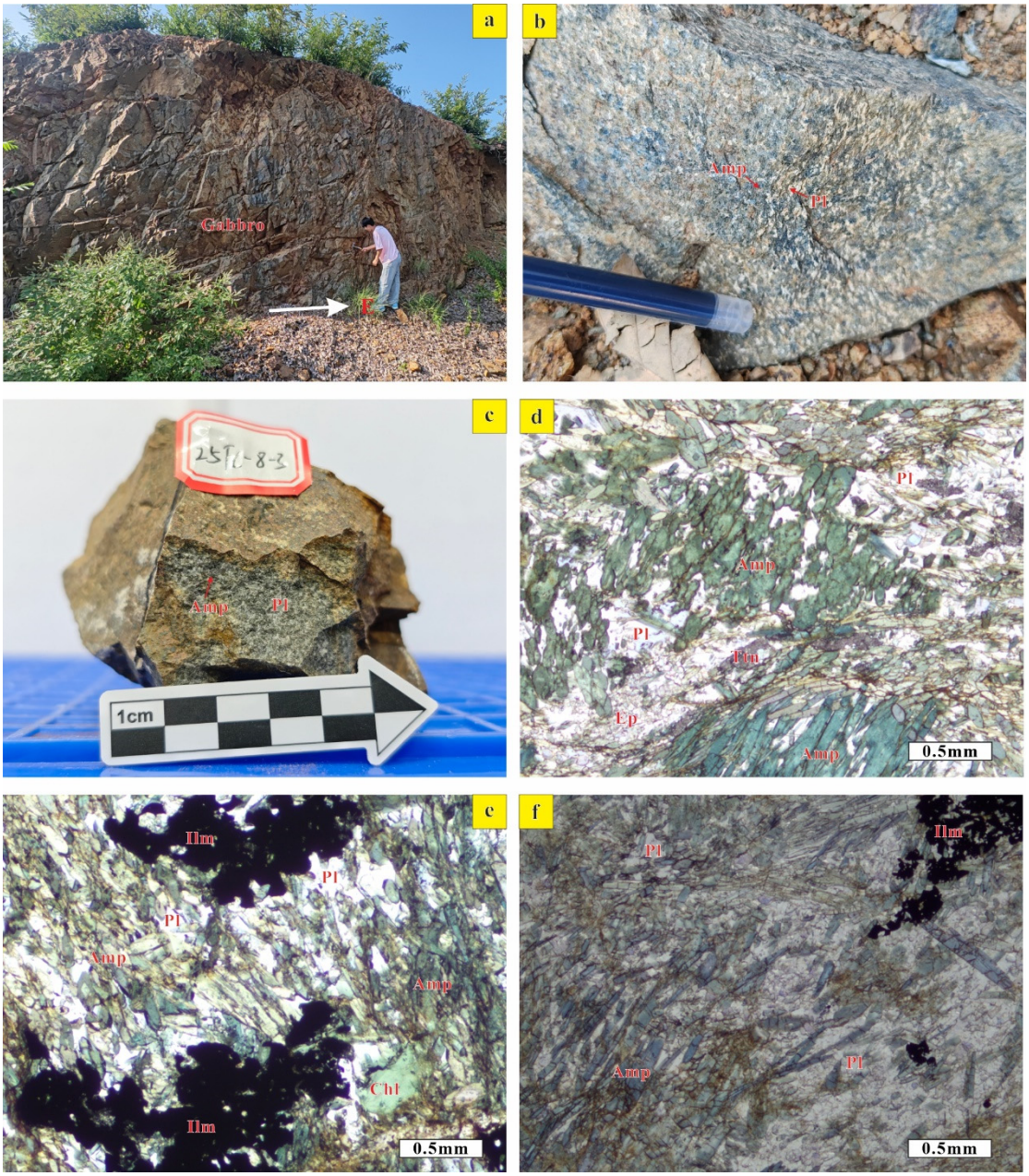


Figure 2. Field photographs and microphotographs of the HM mafic rocks in the SNCC. (**a**) Field outcrop showing the HM mafic rocks with a jointed structure. (**b**) Hand specimen exhibiting dominant plagioclase and amphibole with a metamorphic gabbroic texture. (**c**) Hand specimen with a grayish–green fresh surface but a yellowish–brown joint surface. (**d**) Microphotograph of the mafic rocks in the Nanzhao area showing grayish–green amphibole with a medium-coarse granular texture and minor titanite and epidote with a fine-grained texture. (**e**,**f**) Microphotographs of mafic rocks in the Fangcheng area exhibiting dominant medium-fine plagioclase and columnar amphibole with some primary ilmenite. Mineral abbreviations: Pl–plagioclase; Amp–amphibole; Ilm–ilmenite; Chl–chlorite; Ttn–titanite; Ep–epidote.

4. Analytical Methods

4.1. U–Pb Dating and REE Analyses of Zircons

Zircons were separated from the fresh HM mafic sample (25NZ–5–1, 112°53′51″ E, 33°25′18″ N) using standard heavy-liquid, magnetic techniques, and were handpicked under a binocular microscope. The cathodoluminescence (CL) images coupled with transmitted and reflected light micrographs were obtained at Hebei Chengpu Detection Technology

(Langfang) Co., Ltd, Hebei, China. The U–Th–Pb isotope and rare earth elements of zircons were analyzed at the Hebei Key Laboratory of Strategic Critical Mineral Resources, Hebei GEO University, China, using an ASI™ Resolution–LR Series 193 nm excimer laser ablation instrument (LA) (Coherent, Göttingen, Germany) and Thermo Scientific™ (Shelton, CT, USA) iCAP™ RQ series inductively coupled plasma–mass spectrometry (ICP–MS). The laser beam diameter was 29 μm, the frequency was 6 Hz, and the energy density was 3 J/cm^2. High-purity argon gas was utilized as the denudation carrier, and high-purity He and N_2 gases were utilized to increase sensitivity. The background of ^{204}Pb and ^{202}Hg is usually less than 100 cps. Calibration for the zircon U/Pb ratios and rare earth elements was performed using the Harvard zircon standard 91500 (recommended ^{206}Pb/^{238}U age of 1062 Ma [43]) and the NIST 610, respectively. Plésovice (337 Ma [44]) was utilized to monitor the deviation of ages. Those external standards were alternately tested once for every five samples. The contents of rare earth elements were calculated using ^{29}Si as the internal standard. U–Th–Pb isotopic ratios and concentrations were calculated using iolite ver. 4.3.0. The common lead of zircon was corrected following the method of Anderson [45]. The ages were calculated using the IsoplotR 6.7 software [46]. Data errors are reported at 2σ, while the weighted average age error is given at 95% confidence. The U–Th–Pb isotopic data and rare earth element contents of zircons are listed in Tables 1 and 2, respectively.

4.2. Geochemistry Analyses of the HM Gabbros

Fresh samples were washed with distilled water in an ultrasonic bath and ground into a 200-mesh powder. Major whole-rock analyses were performed on a wavelength X-ray fluorescence Spectrometer 3080E using fused glass disks at the Guangzhou Topan Testing Technology Co., Ltd, Guangzhou, China. Loss on ignition (LOI) was determined by the gravimetric method. Analytical precision and accuracy were better than 2%. Powdered samples were digested in high-pressure Teflon bombs using a mixture of super-pure HF–HNO_3 for two days at approximately 100 °C. The procedure entailed evaporation to near dryness, refluxing with super-pure HNO_3, and drying twice until the powders were completely dissolved. Trace and rare earth elements were analyzed using an inductively coupled plasma–mass spectrometer (ICP–MS, model ICAPRQ) at the same institution. The test accuracy is approximately 5% for trace elements, with a concentration greater than 10×10^{-6}, and rare earth elements, while the accuracy for elements with a concentration less than 10×10^{-6} is about 10%. The major element and trace element contents of the HM mafic samples are presented in Tables 3 and 4, respectively.

Table 1. LA–ICP–MS zircon U–Pb data for the HM mafic intrusions in the SNCC (25NZ–5–1, 112°53′51″ E, 33°25′18″ N).

Spots	Th/U Ratio	Concentration (ppm)		Isotopic Ratios						Age (Ma)						Concordance
		U	Th	$^{207}Pb/^{206}Pb$	2σ	$^{207}Pb/^{235}U$	2σ	$^{206}Pb/^{238}U$	2σ	$^{207}Pb/^{206}Pb$	2σ	$^{207}Pb/^{235}U$	2σ	$^{206}Pb/^{238}U$	2σ	
25NZ5-1@1	0.82	164.70	134.80	0.0576	0.0026	0.4804	0.0205	0.0596	0.0012	494.4	97.9	397.7	14.0	373.3	7.4	−6.55%
25NZ5-1@2	0.50	341.86	170.88	0.0573	0.0036	0.4910	0.0265	0.0615	0.0028	514.5	131.3	405.0	18.2	385.0	16.9	−5.21%
25NZ5-1@3	0.69	222.64	154.29	0.0595	0.0027	0.5088	0.0311	0.0620	0.0023	578.1	94.9	417.2	20.8	387.8	13.9	−7.57%
25NZ5-1@4	0.93	430.71	398.69	0.0584	0.0025	0.5052	0.0216	0.0622	0.0023	558.9	80.4	413.9	14.5	388.5	14.0	−6.51%
25NZ5-1@5	0.78	367.31	285.53	0.0577	0.0025	0.5053	0.0225	0.0626	0.0017	518.7	91.4	414.6	15.2	391.5	10.0	−5.89%
25NZ5-1@6	0.74	193.75	142.61	0.0589	0.0037	0.5014	0.0351	0.0628	0.0017	548.4	125.4	410.7	22.9	392.6	10.4	−4.61%
25NZ5-1@7	1.20	371.65	446.99	0.0547	0.0012	0.4757	0.0268	0.0634	0.0021	397.8	51.0	395.1	18.4	396.3	12.9	0.30%
25NZ5-1@8	0.45	290.21	131.31	0.0577	0.0027	0.5122	0.0274	0.0635	0.0017	551.8	66.3	419.4	18.8	396.9	10.0	−5.68%
25NZ5-1@9	0.40	282.69	113.31	0.0547	0.0022	0.4779	0.0210	0.0639	0.0022	446.2	79.2	395.2	14.2	399.2	13.4	1.01%
25NZ5-1@10	0.47	112.33	52.57	0.0574	0.0035	0.4929	0.0273	0.0651	0.0028	588.3	101.9	409.9	21.5	406.2	17.1	−0.91%
25NZ5-1@11	0.59	180.59	106.65	0.0572	0.0028	0.5178	0.0287	0.0660	0.0021	476.9	102.3	422.5	18.9	412.0	12.9	−2.55%
25NZ5-1@12	0.89	380.31	338.12	0.0583	0.0032	0.5448	0.0370	0.0664	0.0023	552.3	108.3	440.2	24.2	414.5	13.7	−6.20%
25NZ5-1@13	0.90	267.44	241.74	0.0555	0.0023	0.5108	0.0265	0.0669	0.0018	449.7	81.1	417.7	17.7	417.4	10.8	−0.05%
25NZ5-1@14	0.40	169.75	67.45	0.0581	0.0025	0.5355	0.0254	0.0673	0.0027	575.0	79.3	433.4	16.9	419.3	16.0	−3.37%

Table 2. REE concentration of zircons for the HM mafic intrusions in the SNCC (25NZ–5–1, 112°53′51″ E, 33°25′18″ N).

Spots	La	Ce	Pr	Nd	Sm	Eu	Gd	Tb	Dy	Ho	Er	Tm	Yb	Lu	∑REE	Ce*	Eu*
25NZ5-1@1	0.15	5.94	0.20	1.73	3.89	0.81	26.74	10.39	155.79	62.14	320.53	74.16	716.99	146.43	1525.89	8.26	0.24
25NZ5-1@2	0.15	12.51	0.19	1.98	5.50	1.04	32.38	11.78	163.46	63.58	317.39	65.13	605.01	119.63	1399.73	17.90	0.24
25NZ5-1@3	0.17	11.65	0.14	2.22	3.96	0.88	23.88	8.82	121.97	49.15	250.22	54.53	516.54	100.32	1144.45	17.88	0.27
25NZ5-1@4	0.18	8.76	0.25	2.70	3.90	0.84	21.19	7.88	113.81	44.46	225.33	48.82	462.99	91.95	1033.06	10.11	0.28
25NZ5-1@5	0.25	6.07	0.28	2.36	3.19	0.69	23.53	9.02	121.79	45.85	234.74	53.40	496.36	93.04	1090.56	5.58	0.24
25NZ5-1@6	0.26	11.63	0.20	1.96	4.83	0.82	31.77	12.41	163.46	66.97	348.73	73.71	681.77	136.61	1535.15	12.17	0.20
25NZ5-1@7	0.31	15.75	0.24	2.09	4.58	1.10	22.28	9.45	123.54	50.83	253.41	52.27	493.88	98.01	1127.74	14.05	0.33
25NZ5-1@8	0.39	5.31	0.18	2.01	3.99	0.64	24.16	9.77	135.49	55.29	274.50	62.80	590.19	112.63	1277.36	4.85	0.20
25NZ5-1@9	0.43	11.02	0.18	2.01	4.82	0.58	26.89	9.98	148.27	59.23	305.53	73.02	687.06	140.87	1469.86	9.74	0.16
25NZ5-1@10	0.51	10.75	0.45	3.28	3.61	0.53	23.61	9.12	123.48	50.94	267.20	58.00	537.37	113.12	1201.98	5.46	0.18
25NZ5-1@11	0.84	14.63	0.43	3.19	5.03	0.73	27.09	10.42	146.29	59.68	310.09	72.15	680.74	135.38	1466.69	5.87	0.19
25NZ5-1@12	1.06	15.72	0.86	4.32	4.97	0.90	28.38	9.91	132.86	54.14	281.32	61.12	551.05	115.51	1262.11	3.99	0.23
25NZ5-1@13	1.73	13.44	0.53	3.31	3.82	0.64	22.48	7.87	116.07	45.73	238.11	51.42	472.75	92.67	1070.57	3.39	0.21
25NZ5-1@14	1.82	15.15	0.50	3.18	4.47	0.79	26.26	10.33	135.10	53.20	268.32	57.38	529.24	105.08	1210.82	3.85	0.22

Note: $Ce^* = Ce_N/(La_N \times Pr_N)^{0.5}$; $Eu^* = Eu_N/(Sm_N \times Gd_N)^{0.5}$; CI chondrite-norm data after [47].

Table 3. Major element compositions (wt%) and CIPW normative minerals of the HM mafic intrusions in the SNCC.

Sample No.	25FC-5-1	25FC-5-2	25FC-5-3	25NZ-8-1	25NZ-8-2	25NZ-8-3	25NZ-8-4	25NZ-8-5	25NZ-8-6
Locality	Maogudui 112°53′51″ E 33°25′18″ N		Dongkelaao 112°53′42″ E 33°25′36″ N	Chongxingsi 112°39′27″ E 33°29′13″ N				Liujiazhuang 112°41′09″ E 33°28′46″ N	
Petrology	Olivine gabbronorite	Gabbroniotite	Olivine gabbro	Gabbronorite	Gabbronorite	Gabbronorite	Gabbronorite	Gabbronorite	Gabbronorite
SiO_2	49.71	49.98	48.94	50.83	51.64	51.57	51.70	50.95	50.05
TiO_2	1.56	1.42	1.61	1.53	1.56	1.50	1.50	1.57	1.26
Al_2O_3	14.00	13.91	14.08	13.76	12.92	13.56	13.55	13.81	13.78
Fe_2O_3t	13.87	13.32	14.37	13.31	13.57	13.49	13.44	12.22	12.28
FeOt	12.48	11.99	12.93	11.98	12.21	12.14	12.09	11.00	11.05
MnO	0.19	0.19	0.20	0.20	0.18	0.20	0.20	0.20	0.18
MgO	7.13	6.75	6.61	5.96	6.24	6.27	6.25	6.52	6.73
CaO	9.21	10.59	10.23	10.62	10.08	9.29	9.26	10.31	10.35
Na_2O	2.77	2.31	3.19	1.60	1.46	2.21	2.20	2.63	2.54
K_2O	0.14	0.15	0.34	0.22	0.15	0.22	0.22	0.41	0.35
P_2O_5	0.12	0.14	0.14	0.12	0.13	0.12	0.12	0.12	0.11
LOI	1.05	0.97	0.99	1.57	1.80	1.30	1.30	0.90	0.98
Total	99.76	99.72	99.71	99.72	99.72	99.73	99.74	99.65	99.62
ALK	2.91	2.46	3.53	1.83	1.61	2.43	2.42	3.05	2.88
Mg#	50.70	50.32	47.92	47.23	47.91	48.17	48.20	51.62	52.30
σ	1.26	0.87	2.10	0.43	0.30	0.69	0.67	1.17	1.18
AR	1.29	1.22	1.34	1.16	1.15	1.24	1.24	1.29	1.27
CIPW weight norm									
Quartz				5.30	7.61	3.98	4.23		
Plagioclase	50.17	47.94	51.01	44.69	42.03	46.46	46.40	48.12	48.40
Orthoclase	0.83	0.89	2.01	1.36	0.95	1.36	1.36	2.48	2.13
Diopside	16.65	20.86	22.72	19.12	18.10	16.17	16.05	21.94	21.87
Hypersthene	22.68	26.66	2.45	26.23	27.93	28.79	28.73	23.98	22.29
Olivine	6.34	0.54	18.37					0.13	2.56
Ilmenite	3.04	2.77	3.11	3.00	3.08	2.94	2.92	3.06	2.49
Apatite	0.30	0.35	0.32	0.30	0.30	0.30	0.30	0.28	0.28
Total	100.01	100.01	100.01	100.00	100.00	100.00	99.99	99.99	100.01

Notes: All oxides in weight %; LOI loss on ignition; FeOt = 0.8998 × Fe_2O_3t; ALK = Na_2O + K_2O; Mg# = 100 × Mg/(Mg + Fe^{2+}); σ = $ALK^2/(SiO_2\text{-}43)$; AR = (Al_2O_3 + CaO + ALK)/(Al_2O_3 + CaO-ALK).

Table 4. Trace and rare earth element ($\times 10^{-6}$) compositions of the HM mafic intrusions in the SNCC.

Sample No.	**25FC-5-1**	**25FC-5-2**	**25FC-5-3**	**25NZ-8-1**	**25NZ-8-2**	**25NZ-8-3**	**25NZ-8-4**	**25NZ-8-5**	**25NZ-8-6**
Locality	Maogudui 112°53′51″ E 33°25′18″ N		Dongkelaao 112°53′42″ E 33°25′36″ N	Chongxingsi 112°39′27″ E 33°29′13″ N				Liujiazhuang 112°41′09″ E 33°28′46″ N	
Petrology	Olivine gabbronorite	Gabbroniotite	Olivine gabbro	Gabbronorite	Gabbronorite	Gabbronorite	Gabbronorite	Gabbronorite	Gabbronorite
Li	8.7	8.6	7.4	6.7	7.4	7.6	7.4	17.5	18.2
P	493	576	611	485	556	528	512	494	463
Sc	43.1	42.9	44.3	39.7	42.1	41.3	40.3	38.0	35.1
Ti	7339.5	6596.6	8008.1	7100.7	7873.2	7690.4	7352.2	7705.9	5747.2
V	305	320	317	318	302	306	303	274	243
Cr	174	159	133	122	127	135	136	127	102
Mn	1448	1431	1564	1455	1404	1568	1507	1530	1370
Co	42.5	41.8	49.5	35.1	41.5	41.8	40.7	47.4	27.2
Ni	69.7	78.7	80.8	59.6	59.3	60.7	59.7	60.5	61.9
Rb	1.9	2.7	3.5	5.2	3.2	5.3	5.1	7.9	6.6
Sr	98.8	193.4	251.8	318.9	242.6	244.2	238.3	256.3	234.7
Y	24.2	25.9	29.3	24.6	26.9	27.1	25.6	20.7	18.4
Zr	81	82	98	79	89	83	80	71	71
Nb	3.9	5.5	5.4	4.3	4.5	4.4	4.3	4.2	3.3
Cs	0.13	0.20	0.20	0.18	0.12	0.16	0.16	0.61	0.54
Ba	68.5	73.3	119.3	70.8	80.8	81.6	78.4	242.2	167.4
Hf	2.2	2.3	2.7	2.2	2.5	2.4	2.3	2.1	1.9
Ta	0.30	0.37	0.38	0.34	0.32	0.34	0.34	0.30	0.28
Pb	0.9	1.1	1.3	3.0	4.2	3.0	2.8	6.3	5.2
Bi	0.01	0.03	0.02	0.03	0.02	0.02	0.02	0.10	0.04
Th	0.40	0.41	0.49	0.37	0.43	0.40	0.38	0.37	0.36
U	0.14	0.13	0.16	0.16	0.18	0.17	0.17	0.38	0.22
La	4.9	5.7	5.4	4.3	5.4	4.9	4.9	4.0	3.3
Ce	13.2	14.0	15.5	11.8	14.6	13.8	13.2	11.5	10.0
Pr	2.22	2.28	2.48	2.04	2.41	2.32	2.27	1.98	1.63
Nd	10.9	11.7	12.1	10.2	11.7	11.2	10.8	9.6	8.8
Sm	3.27	3.47	4.12	3.07	3.82	3.80	3.63	3.11	2.48
Eu	1.32	1.47	1.43	1.35	1.32	1.36	1.38	1.15	0.93

Table 4. *Cont.*

Sample No.	25FC-5-1	25FC-5-2	25FC-5-3	25NZ-8-1	25NZ-8-2	25NZ-8-3	25NZ-8-4	25NZ-8-5	25NZ-8-6
Gd	3.95	4.15	4.83	3.69	4.41	4.46	4.22	3.41	3.19
Tb	0.72	0.76	0.84	0.72	0.79	0.82	0.79	0.64	0.56
Dy	4.65	5.01	5.40	4.57	4.86	4.86	4.66	3.83	3.83
Ho	0.96	0.98	1.16	0.96	1.06	1.08	1.02	0.83	0.72
Er	2.67	2.80	2.94	2.73	2.61	2.62	2.65	2.23	2.15
Tm	0.42	0.44	0.52	0.40	0.45	0.45	0.43	0.37	0.34
Yb	2.72	2.83	3.11	2.71	2.76	2.83	2.86	2.42	2.13
Lu	0.37	0.40	0.44	0.39	0.38	0.38	0.37	0.32	0.33
∑REE	52.28	55.98	60.30	48.93	56.54	54.79	53.20	45.36	40.31
$(La/Yb)_N$	1.22	1.36	1.18	1.08	1.32	1.17	1.16	1.11	1.05
$(La/Sm)_N$	0.93	1.02	0.82	0.88	0.88	0.80	0.84	0.80	0.83
$(Gd/Yb)_N$	1.18	1.19	1.26	1.10	1.29	1.28	1.20	1.14	1.21
δEu	1.12	1.18	0.97	1.22	0.98	1.01	1.07	1.08	1.00

Notes: Trace elements and rare earth elements are in μg/g; chondrite-norm data after [47].

5. Results

5.1. Zircon Texture, Trace Elements, and U–Pb Ages

Zircon grains of the HM mafic sample (25NZ–5–1, 112°53′50.97″ N, 33°25′17.96″ E) are generally euhedral to subhedral, with crystals of approximately 60–80 μm in length and 50–70 μm in width. Most of them exhibit typical wide growth zoning or weak oscillatory zoning (Figure 3a) and have relatively high Th/U ratios (Figure 3b and Table 1, 0.4–1.2, generally >0.1, [48]), which is indicative of magmatic zircons [49,50]. In the chondrite–normalized REE diagram (Figure 3b), all the zircons show typical positive Ce anomalies (δCe = 3.39–17.90) and negative Eu anomalies (δEu = 0.16–0.28). These indicate the characteristics of mantle-derived magmatic zircon [50–52]. Fourteen analyses form a concordant cluster, yielding a mean $^{206}Pb/^{238}U$ age of 397.5 ± 3.5 Ma (MSWD = 2.9; Figure 3a,b and Table 1), belonging to the Early Devonian, which is interpreted as the crystallization age of the HM mafic intrusions.

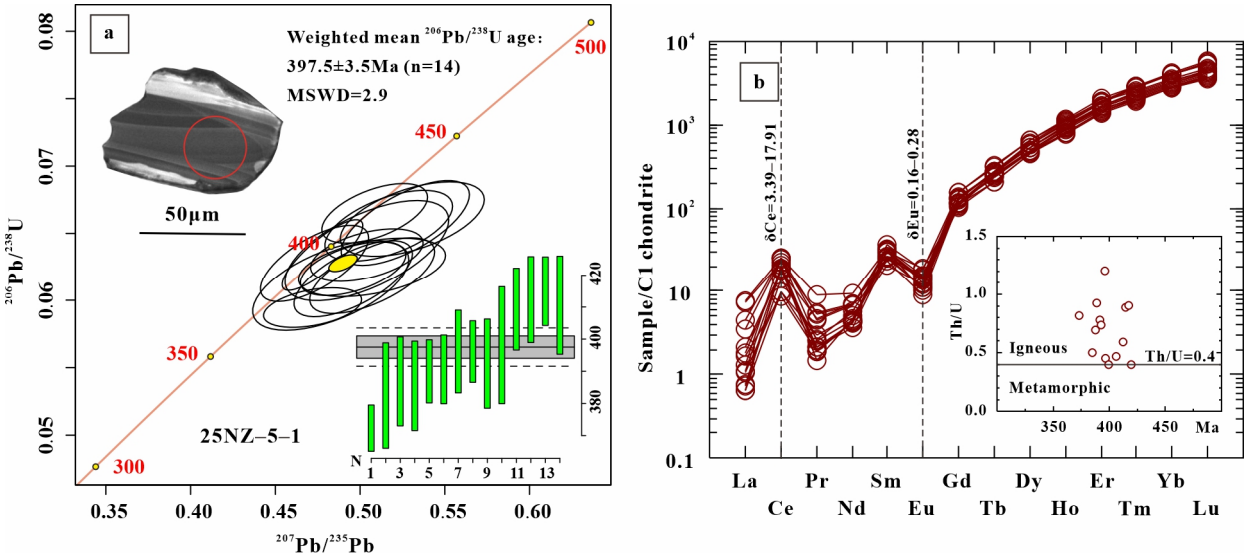


Figure 3. (**a**) LA–ICP–MS zircon U–Pb concordia diagrams and weighted mean $^{206}Pb/^{238}U$ ages of zircon grains with representative CL images of wide growth zoning or weak oscillatory zoning from the HM mafic sample (25NZ–5–1); (**b**) Th/U ratios versus ages and the chondrite-normalized REE diagrams indicating the characteristics of mantle-derived magmatic zircon. Chondrite-normalized data after [47].

5.2. Whole-Rock Geochemistry

The HM mafic samples have similar whole-rock geochemical compositions. These samples contain 48.94–51.51 wt% SiO_2, 1.26–1.61 wt% TiO_2, 5.96–7.13 wt% MgO, and 11.00–12.48 wt% FeOt. The total alkali contents (ALK = $Na_2O + K_2O$) range from 1.61 wt% to 3.53 wt%, with $Mg^{\#}$ values of 47.23–52.30 (Table 3). The HM mafic samples are concentrated in the gabbro and gabbroic diorite regions in the total alkali versus silica diagram (Figure 4a, [53]), and in the gabbro, gabbro–norite and gabbro–diorite regions in the R_1–R_2 diagram (Figure 4b, [54]). They are consistent with the results of the CIPW calculation (Table 3). The HM mafic samples are also classified as belonging to the tholeiitic series in the SiO_2 versus FeOt/MgO ratios (Figure 4c, [55]) and ALK–FeOt–MgO (AFM, Figure 4d, [56]) diagrams.

In the chondrite-normalized REE distribution diagram, the HM mafic samples exhibit nearly flat patterns and no typical Eu anomalies (δEu = 0.97–1.22, with an average of 1.07, Table 4). They possess $(La/Sm)_N$ ratios ranging from 0.82 to 1.02, $(La/Yb)_N$ ratios from 1.05 to 1.36, and $(Gd/Yb)_N$ ratios from 1.10 to 1.29 (subscript N denotes chondrite normalization [47]). These characteristics are nearly consistent with those of N–MORB and

E–MORB, but contrast with the typical OIB (Figure 5a). In the primitive mantle-normalized multi-element diagram, the HM mafic samples exhibit enrichment in Ba, U, and Pb, while showing a weak depletion in Ti (Figure 5b).

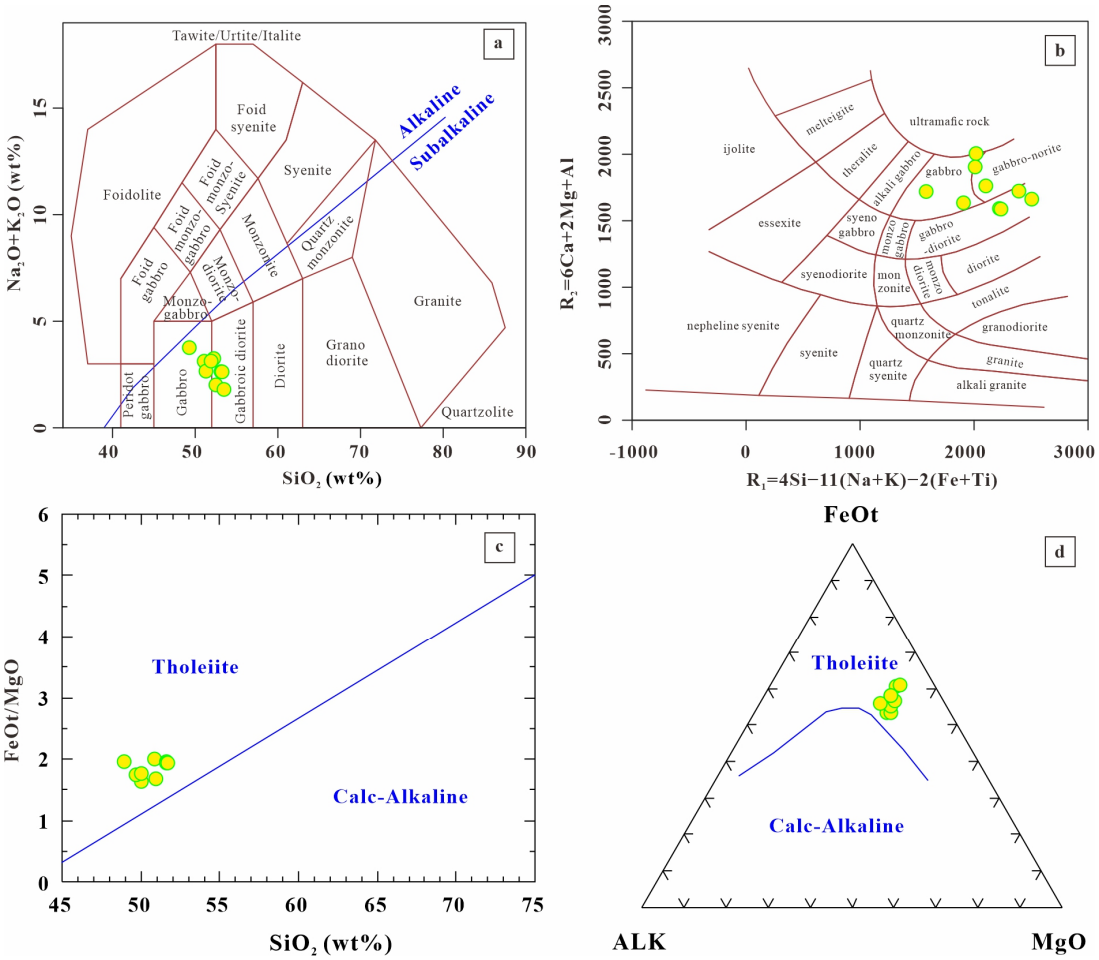


Figure 4. Discrimination diagrams of the HM mafic samples in the SNCC. (**a**) TAS diagram (after [53]). The samples plot within the gabbro and gabbroic diorite fields; (**b**) R_1 vs. R_2 diagram (after [54]). The samples plot within the gabbro, gabbro–norite and gabbroic diorite fields; (**c**) SiO_2 vs. FeOt/MgO ratios. The boundary line between tholeiitic and calc–alkaline series from [55]; (**d**) AFM diagram with the boundary between tholeiite and calc–alkaline series [56].

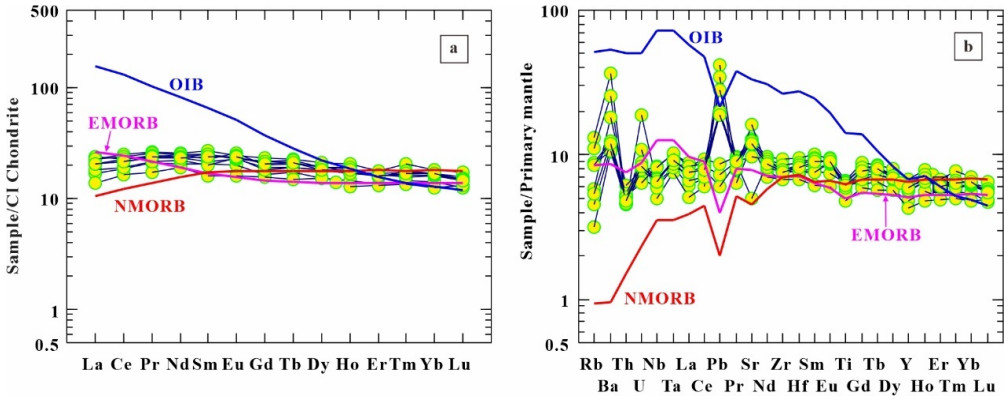


Figure 5. (**a**) Chondrite-normalized REE patterns and (**b**) primitive mantle-normalized trace element patterns for the HM mafic rocks. Chondrite and primitive mantle-normalized values are from [47].

6. Discussion

6.1. Petrogenesis and Magma Source

6.1.1. Effect of Alteration

Field and petrographic observations show that the HM mafic intrusions underwent a certain degree of amphibolization, saussuritization, chloritization, and epidotization (Figure 2). The whole-rock compositions may be influenced by the aforementioned deuteric alterations. Accordingly, an assessment of alteration influences upon whole-rock compositions is inevitable when discussing the petrogenesis of the HM mafic rocks [57,58]. Zirconium (Zr) features limited elemental mobility under alteration and metamorphism [59,60]. The TiO_2, Hf, Th, La, Sm, Yb, Y, Nb, and Ta concentrations of the HM mafic samples in this study show high correlations with Zr (Figure 6a–i). Such evidence indicates that post-magmatic and hydrothermal alterations exerted little disturbance on these elements. Low loss on ignition values (LOI = 0.90–1.80 wt%) coupled with indistinctive Eu anomalies (δEu = 0.97–1.22) in all samples suggest a minimal hydrothermal overprint [61]. Hence, the incompatible elements and their inter-element ratios can serve as effective tracers for the origin and evolution of HM mafic rocks.

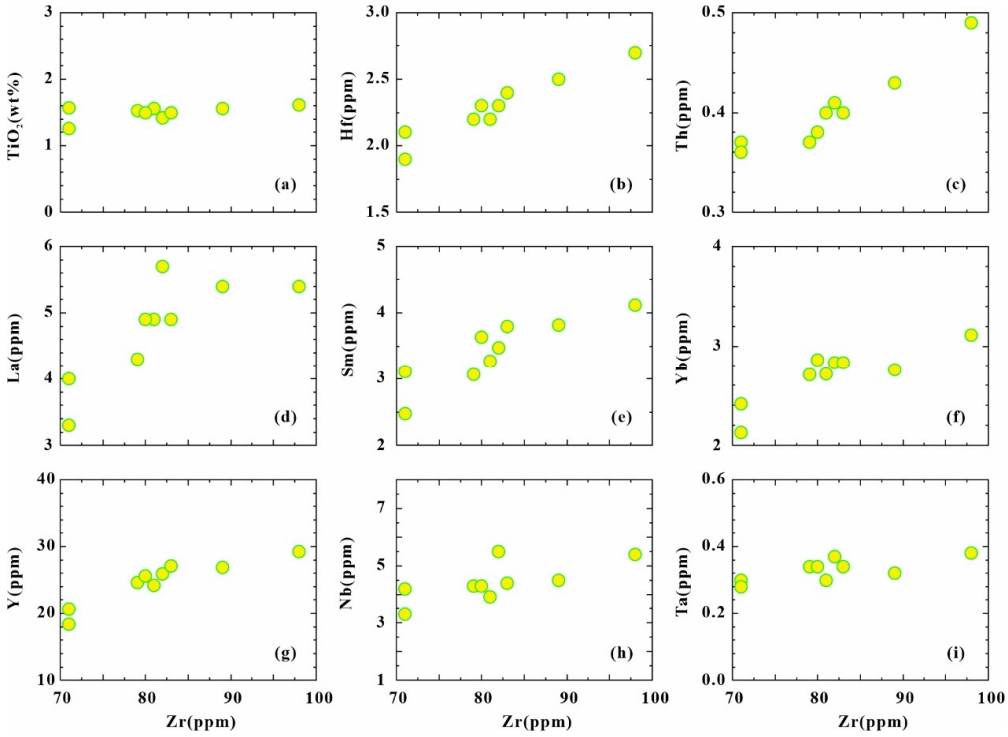


Figure 6. Zr vs. selected element variation diagrams to highlight the effects of alteration (after [61]). (**a**–**i**) Strong correlations between Zr and TiO_2, Hf, Th, La, Sm, Yb, Y, Nb, and Ta indicate that these elements were not significantly disturbed by alteration.

6.1.2. Crustal Contamination and Fractional Crystallization

Mafic magmas originate from the mantle and may be contaminated by the continental crust during their ascent [62]. Therefore, an estimate of crustal contamination overprint on initial magma compositions is essential [24,25]. In contrast with mantle-derived melts, average continental crust has higher LREEs, as well as Zr and Hf contents, but lower Nb and Ta contents, and thus, lower Nb/La and Sm/Nd ratios [63]. Consequently, crustal contamination will lead to positive Zr and Hf anomalies and reduced Nb/La and Sm/Nd ratios with rising SiO_2 contents [24]. The REE distribution pattern and multi-element spider diagrams of the HM mafic samples show no typical LREE enrichment and positive Zr and Hf anomalies (Figure 5a,b). The SiO_2 contents show ambiguous correlation with the

Nb/La and Sm/Nd ratios in the HM mafic samples (Figure 7a,b). This evidence indicates insignificant crustal contamination.

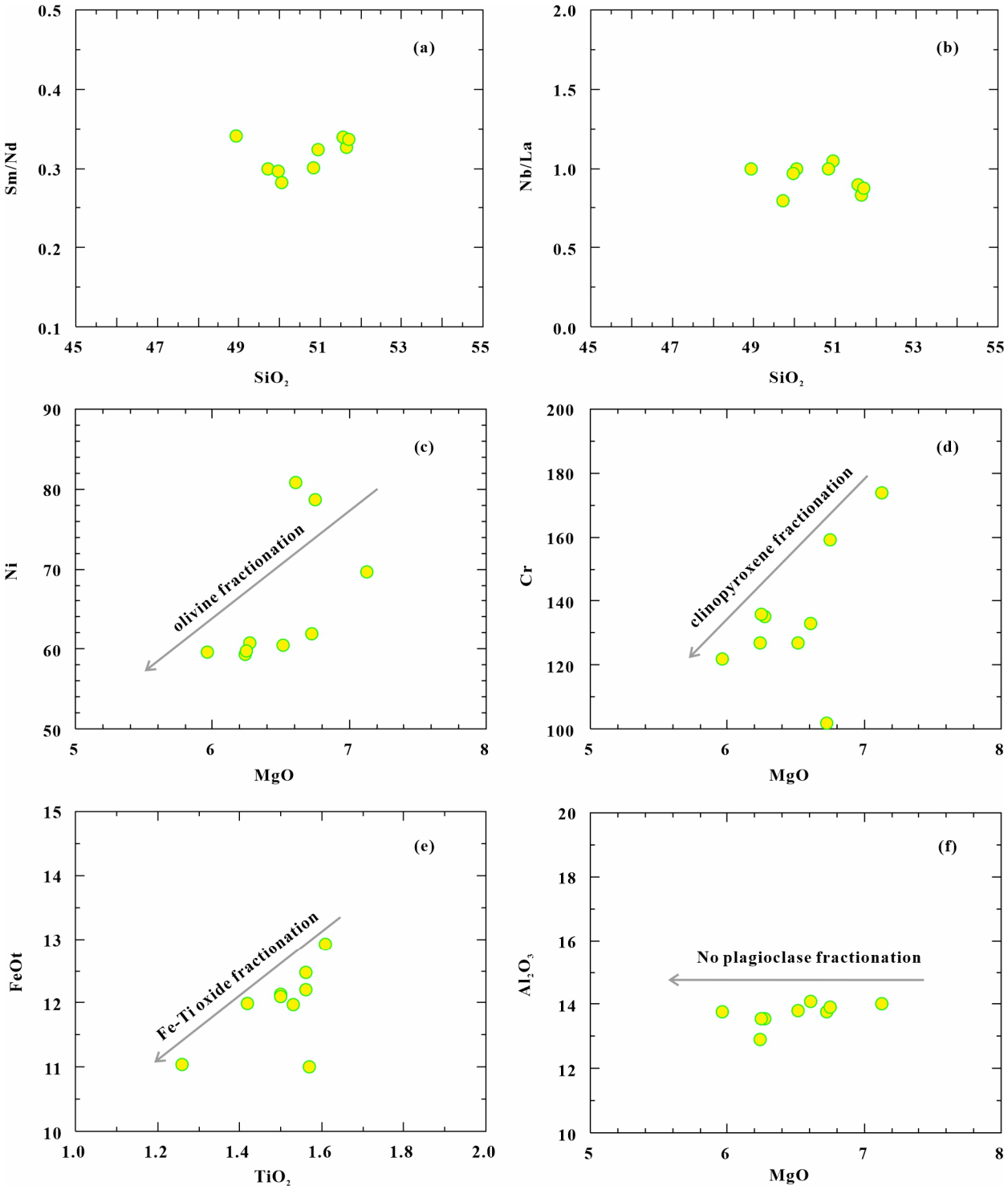


Figure 7. Plots of SiO_2 versus Sm/Nd (**a**) and Nb/La (**b**) indicate insignificant crustal contamination due to the lack of a clear correlation between them. Plots of MgO versus Ni (**c**) and Cr (**d**) showing that the olivine and clinopyroxene have undergone fractionation based on positive correlations. Plots of TiO_2 versus FeOt (**e**) indicate fractionation of Fe–Ti oxides based on positive correlation, while MgO versus Al_2O_3 (**f**) precludes plagioclase as a major fractionation phase based on the observed weak correlation.

The MgO (5.96–7.13 wt%), Cr (102–174 ppm), and Ni (59–81 ppm) contents and $Mg^{\#}$ values (47.23–52.30) are relatively lower than those of primary magmas (Mg# = 65–73, Cr > 300–400 ppm, Ni > 295–500 ppm; [64]). Such geochemical features indicate partial fractional crystallization of the HM mafic rocks. The variable Ni and Cr contents correlate positively with the MgO content (Figure 7c,d), which are indicative of olivine and clinopyroxene fractionation, respectively. The positive correlation between FeOt and TiO_2 indicates the fractionation of Fe–Ti oxides (Figure 7e). The observed weak correlations of CaO/Al_2O_3 and CaO with MgO (Figure 7e,f) preclude plagioclase as a major fractionation phase, and these correlations are consistent with the absence of Eu anomalies (Figure 5a). Combined with the petrographic results, the HM mafic intrusions underwent fractionation of mainly olivine, clinopyroxene, and minor Fe–Ti oxides, but almost no plagioclase.

6.1.3. Nature of the Mantle Source

Variations in MgO (5.96–7.13 wt%) and SiO_2 (48.94–51.70 wt%) contents of the HM mafic samples suggest that a derivation from partial melting of an ultramafic mantle reservoir [64]. The normal asthenospheric mantle is depleted in incompatible trace elements [65]. In contrast, the lithospheric mantle may be refractory or fertile in major element compositions, and enriched or depleted in incompatible trace elements [66]. Therefore, incompatible trace elements (e.g., Zr and Nb) are employed to discriminate the nature of the magma source and reveal mantle-source enrichment or depletion [57,67]. The HM mafic samples exhibit low Nb concentrations, accompanied by low Zr concentrations. This indicates the characteristics of the depleted mantle, similar to the post-collisional gabbro (Figure 8a). As suggested above, the depleted component can be interpreted as the asthenosphere mantle, whereas the enriched component may be the lithosphere mantle because continental crustal signatures, such as depletion of Zr and Hf, are absent [64]. These geochemical signatures can be interpreted in terms of a mixed mantle source involving asthenosphere and lithosphere components, which is also revealed by the variable Nb/La ratios (0.81–1.06, Figure 8b, [64]) and little LILE enrichment (Figure 5b). The REE pattern is quite flat (La/Yb = 1.05–1.36, with an average of 1.18; Figure 5a), indicating that no residual garnet remained in the source. In the Tb_N/Yb_N versus La_N/Sm_N diagram, all the HM mafic samples fall into the spinel stability domain (Figure 8c), as previously suggested (Figure 5a). In the Th/Yb versus Ta/Yb plot, data points of the HM mafic rocks fall along the oceanic mantle array field spanning from N–MORB to E–MORB (Figure 8d). This also indicates the involvement of asthenospheric mantle in their genesis [68]. The lower Th/Yb ratios rule out contributions from subduction constituents during partial melting, as well as contamination of middle and lower crustal materials in the formation and evolution of these mafic intrusions (Figure 8d).

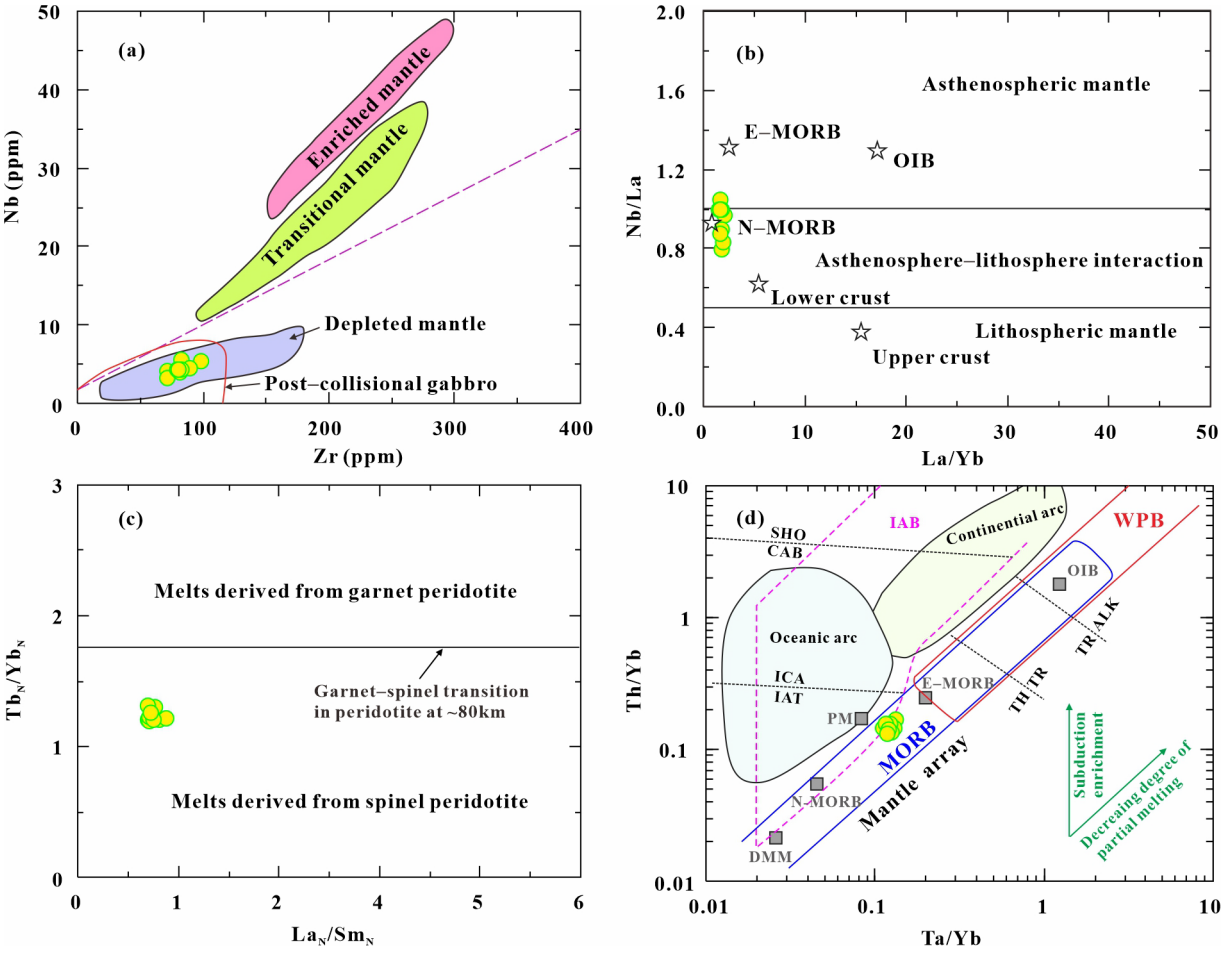


Figure 8. (**a**) Zr versus Nb diagram [67]. The post-collisional gabbro is used for comparison [69]. (**b**) Nb/La versus La/Yb diagram (after [64,70]). (**c**) Chondrite-normalized Tb_N/Yb_N versus La_N/Sm_N diagram (after [71]). (**d**) Th/Yb versus Ta/Yb log–log diagram (modified from [64,68,72,73]). Compositional fields: TH, tholeiitic; TR, transitional; ALK, alkaline; IAT, island arc tholeiitic; ICA, island calc–alkaline; CAB, calc–alkaline basalt; IAB, island arc basalt; SHO, shoshonitic; WPB, within-plate basalt; MORB, mid-ocean ridge basalt; DMM, depleted MORB mantle; PM, primary mantle; OIB, oceanic island basalt; N–MORB, normal mid-oceanic ridge basalt; E–MORB, enriched mid-ocean ridge basalt. Data for PM, N–MORB, E–MORB, and OIB are from [52], DMM from [74], and lower crust and upper crust from [63].

6.1.4. Partial Melting of the Mantle Source

The concentrations of the highly incompatible element (La) and the less incompatible element (Sm) are insignificantly affected by variations in the source mineralogy (e.g., garnet or spinel) and thus can provide information on the bulk chemical composition of the source [72]. Therefore, REE contents and their ratios can constrain the mafic magma provenance, the source mineralogy, and the partial melting intensity [72]. The depleted MORB mantle (DMM) is assumed to represent the convective asthenospheric mantle with the composition of the hypothetical depleted MORB source [75]. The primitive mantle (PM) is representative of the initial mantle composition prior to MORB formation [52]. A mantle source (WAM) has been enriched in LREE relative to DMM and PM, and it is inferred to produce the alkaline magma, OIB, and E–MORB [72] (Figure 9a). In the La/Sm versus La diagram, the HM mafic samples have La concentrations and La/Sm ratios close to those of N–MORB but lower than those of the OIB and E–MORB, indicating a depleted mantle source and a ~5% degree of partial melting (Figure 9a). Meanwhile, the lower Sm/Yb ratios suggest that the source of the HM mafic samples may be depleted spinel

lherzolite. The Sm concentrations range from 2.48 to 4.12, with an average of 3.42, which is close to those of E–MORB and N–MORB (2.63 and 2.60, respectively; [47]), indicating a ~5–10% degree of partial melting (Figure 9b). The HM mafic rocks had lower La/Yb (1.05–1.36) ratios than the Silurian gabbros (1.88–7.00, [24]) and the mafic dikes of the Erlangping unit (6.04–20.80, [19,76]). To sum up, the HM mafic intrusions originated from decompression partial melting of the depleted spinel asthenospheric mantle at relatively low-pressure conditions.

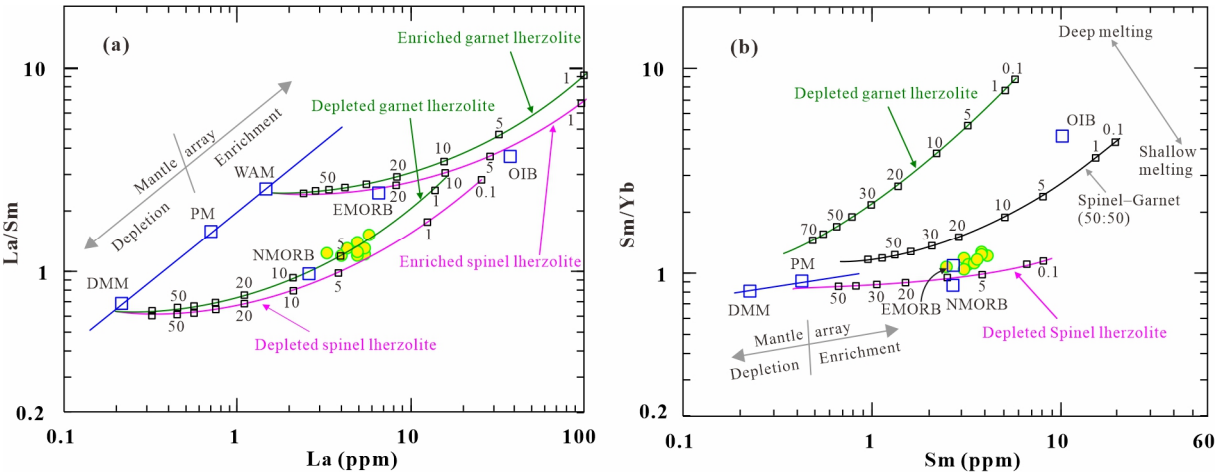


Figure 9. Plots of La/Sm vs. La (**a**) and Sm/Yb vs. Sm (**b**) (modified from [72]) showing melt curves obtained using the non-modal batch melting equation [77]. Melt curves are presented for spinel–lherzolite [78] and garnet lherzolite [79]. Mineral/matrix partition coefficients are from [75]. Curves illustrate the melting trend, and the symbols distributed on every curve stand for partial melting extents (%) of an assigned mantle source. The depleted mantle source refers to depleted mantle (DM) or depleted MORB mantle (DMM), while the inferred mantle source (WAM) refers to enriched mantle [75].

6.2. Tectonic Setting

The HM mafic intrusions exhibit flat REE patterns and have a close affinity with MORB (Figure 5a,b). They plot within the region of the oceanic mantle array between N–MORB and E–MORB (Figure 8d). In the Ti–Zr diagram [80] and the Nb–Zr–Y diagram [81], the HM mafic intrusions also exhibit MORB-like trace element features (Figure 10a,b). The immobile trace elements such as La, Sm, Yb, Nb, and Th are employed, along with ratios such as La/Th, Sm/Th, Yb/Th, and Nb/Th, to discriminate the tectonics of mafic and ultramafic rocks [82]. Based on the DF1 and DF2 parameters [82], the HM mafic intrusions are clustered in the MORB field and display a stronger affinity with E–MORB and PM (Figure 10c–f). Furthermore, these discriminant tectonic setting diagrams also confirm the absence of typical arc signatures (Figure 10c–f), which are also indicated by the trace spider diagram (Figure 5b) and low Th/Yb (Figure 8d). Generally, MORB-like geochemistry is a direct product of the melting of a depleted mantle source under specific pressure–temperature conditions in extensional tectonic settings [83]. Therefore, the HM mafic intrusions are proposed to typically originate in a continental extensional environment due to the upwelling of the hot asthenosphere, which is observed in the Alpine–Apenninic collisional orogenic belt [84,85].

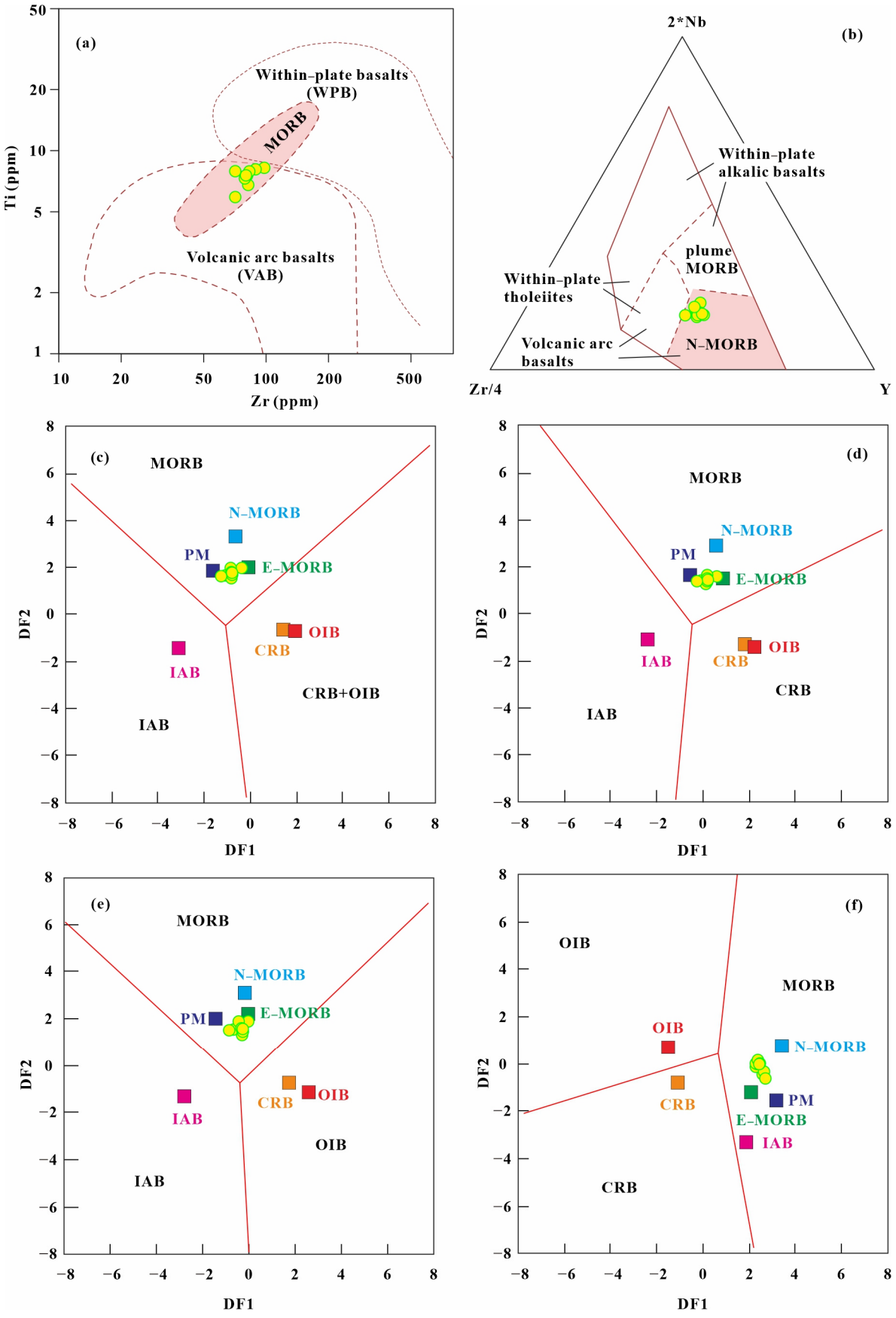


Figure 10. Tectonic discrimination diagrams for the HM mafic intrusions in the SNCC. (**a**) Ti–Zr diagram [80]; (**b**) 2*Nd–Zr/4–Y diagram [81]; (**c**–**f**) discriminant function diagrams based on immobile trace elements (La, Sm, Yb, Nb, and Th). The two function equations of DF1 and DF2 are from [82].

6.3. Implications for Tectonic Evolution and Regional Mineralization

The tectonic evolution of the SNCC and the Qinling Orogen has been systematically investigated, and numerous reported geochronological data for the magmatic and metamorphic rocks have been compiled [24,25,27,28,32,86,87]. Neoproterozoic mafic rocks (e.g., Zhouzhuang gabbro, 859 Ma, and Luanchuan gabbro, 830 Ma; Figure 1a) were formed during the rifting-related extension of the Rodinia supercontinent in the SNCC (900–750 Ma; [17,18,27,31]). Subsequently, the breakup of Rodinia and the opening of the Proto–Tethys Shangdan Ocean took place between approximately 750 and 600 Ma, probably generated by an independent mantle plume activity [31,88]. The Songshugou ophiolite along the Shangdan suture is regarded as remnant fragments of the northern segment of the Pro–Tethys Ocean (Figure 1a; [32]). N–MORB-affinity gabbro and plagiogranite dated at ca. 534–471 Ma [23,42,89], together with Cambrian–Ordovician fossil-bearing chert intercalations within volcanic strata, constrain the formation of the Shangdan oceanic crust. Some occurrences of coeval E–MORB-type gabbro (518 ± 3 Ma; [32,90]) and basalt (483 ± 13 Ma [91,92]) have been documented within surrounding regions [25].

The Erlangping back-arc basin is generally acknowledged as a result of the subduction of the Shangdan Ocean beneath the Qinling terrane. However, the precise timing and tectonic evolution are still debated (Figure 11a, [24,27,32,83,86]). Boninite-like diabases with ca. 524 Ma are thought to reflect the subduction initiation [86]. Long-lived subduction is also suggested by abundant subduction-related mafic rocks (ca. 524–438 Ma) [25]. The maximum depositional ages for the fore-arc sedimentary were ca. 455 Ma and ca. 454Ma, which were identified to be the time of the initial back-arc rifting (Figure 11a,b, [24,32]). And the Erlangping back-arc basin gradually matures due to the occurrence of a series of E–MORB-type pillow lavas, dacites, and high-Mg diorites during ca. 448–438 Ma [19,24]. Depositions of clastic strata in the back-arc basin may have lasted until ca. 440 Ma (Figure 11a, [24,25]). The closure of Shangdan Ocean and the Erlangping back-arc basin probably occurred in the period of 441~436 Ma [27,32] or 440~410 Ma [19,24,25,27], together with a lot of adakitic granites [93], high-grade metamorphism [27,94], migmatization [36,41], and coeval leucogranites [23] (Figure 11b).

Extension and collapse generally occur after crustal thickening in orogenesis due to gravitational delamination or asthenosphere upwelling [95]. The intermediate-acid magmatic intrusions (ca. 409–403 Ma) in the North Qinling Orogen are reported to have formed in an extensional process by high-temperature melting of the juvenile crust [93,94]. The contemporaneous HM mafic intrusions (~400 Ma) have formed in this tectonic setting, which is suggested by the ca. 396–378 Ma A-type monzonites and the ca. 385–380 Ma diorites, appinites [25]. Therefore, continental extension in the SNCC and North Qinling Orogen is accompanied by the upwelling of the hot asthenosphere and the gravitational delamination of the lithosphere (Figure 11c). The HM mafic intrusions indicate the end of the Paleozoic Proto–Tethyan orogenic cycle. Paleozoic strategic metal/non-metal minerals and magmatic hydrothermal REE deposits are proposed to have formed under this specific tectonic regime (Figure 11b,c).

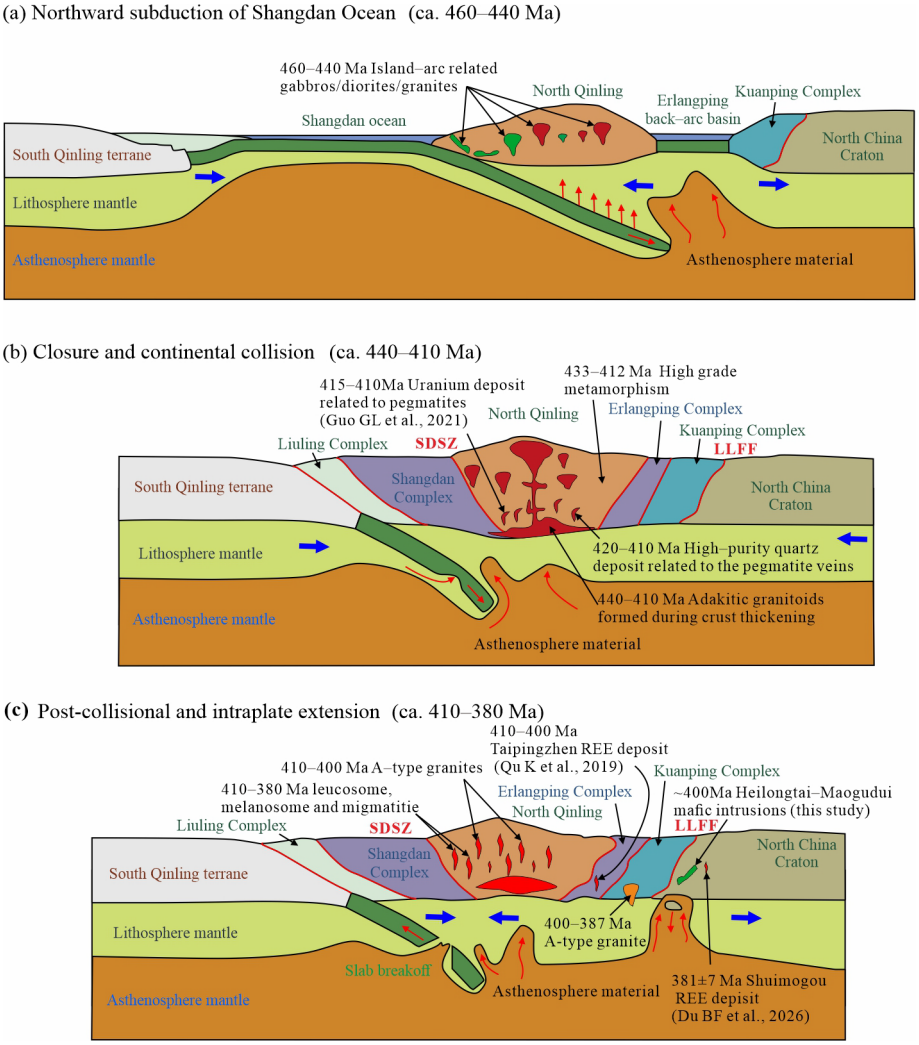


Figure 11. Paleozoic tectonic evolution of the SNCC and the North Qinling Orogen. (**a**) Subduction of the Shangdan ocean beneath the Qinling terrane, subsequently, a mature volcanic arc and the back-arc basin occurred at ca. 460–440 Ma; (**b**) Closure of Shangdan ocean and Erlangping back-arc basin, followed by collision between the North and South Qinling terranes at ca. 440–410 Ma; (**c**) Post-collisional extension at ca. 410–380 Ma, marking the end of the Paleozoic orogenic cycle. Taipingzhen REE deposit, Shuimogou REE deposit, high-purity quartz deposit, and uranium deposit are from [1,3,8,10]. The other data sources are from [25,27,87].

7. Conclusions

New geochronological and geochemical data from the HM mafic intrusions within the SNCC provide the following conclusions:

1. Zircon LA–ICPMS data form a concordant cluster, yielding a mean $^{206}Pb/^{238}U$ age of 397.5 ± 3.5 Ma (MSWD = 2.9), interpreted as the Early Devonian crystallization age. The HM mafic intrusions also indicate the end of the Paleozoic Proto–Tethyan orogenic cycle.
2. The HM mafic intrusions have undergone fractionation of mainly olivine, clinopyroxene, and minor Fe–Ti oxides. The geochemical characteristics exhibit that the HM mafic intrusions belong to the tholeiitic series and display nearly flat REE and trace element patterns that are consistent with MORB.
3. The HM mafic intrusions typically originated in the continental extensional environment through 5–10% degrees of partial melting of the depleted spinel asthenosphere

mantle source due to the gravitational delamination of the lithosphere mantle and the upwelling of the hot asthenosphere.

4. Paleozoic strategic mineral deposits are proposed to have formed under a comparable specific tectonic regime to the HM mafic intrusions.

Author Contributions: Conceptualization, K.L., R.Y., and Y.F.; Methodology, K.L., Y.F., and J.H.; validation, K.L. and Y.F.; formal analysis, Y.F. and J.H.; investigation, Y.F. and P.C.; data curation, K.L., Y.F., J.H., and P.C.; writing—original draft preparation, K.L., Y.F., and J.H.; writing—review and editing, K.L. and Y.F.; supervision, Y.F. and J.H.; funding acquisition, K.L., R.Y., and Y.F. All authors have read and agreed to the published version of the manuscript.

Funding: This research was funded by the Deep Earth Probe and Mineral Resources Exploration–National Science and Technology Major Project (2024ZD1002004), the Metallogenic Mechanism and Prospecting Prediction of Phosphorus and Boron Deposits in China (2023YFC2906600), the Innovation Team for Boron Ore Genesis and Prospecting Technology (ZHTD202403), and the National Natural Science Foundation of China (Nos. 42102039 and 42003033).

Institutional Review Board Statement: Not applicable.

Informed Consent Statement: Not applicable.

Data Availability Statement: Data can be available on request from the corresponding author.

Acknowledgments: Xiaoxiao Huang from North China University of Water Resources and Electric Power is gratefully acknowledged for their help with data interpretation. We also thank Hongshun Yang, Jiaxing Zhou from North China University of Water Resources and Electric Power, and Xinli Chen from Henan Geological Bureau, China Chemical Geology and Mine Bureau, for their field assistance. We are sincerely grateful to the anonymous reviewers who helped improve this paper and to the editors for handling, editing, and advising. The authors have reviewed and edited the output and take full responsibility for the content of this publication.

Conflicts of Interest: The authors declare no conflicts of interest.

References

1. Qu, K.; Sima, X.; Zhou, H.; Xiao, Z.; Tu, J.; Yin, Q.; Liu, X.; Li, J. In situ LA–MC–ICP–MS and ID–TIMS U–Pb ages of bastnäsite–(Ce) and zircon from the Taipingzhen hydrothermal REE deposit: New constraints on the later Paleozoic granite–related U–REE mineralization in the North Qinling Orogen, Central China. *J. Asian Earth Sci.* **2019**, *173*, 352–363. [CrossRef]
2. Zhang, W.; Chen, W.T.; Gao, J.F.; Chen, H.K.; Li, J.H. Two episodes of REE mineralization in the Qinling Orogenic Belt, Central China: In–situ U–Th–Pb dating of bastnäsite and monazite. *Miner. Depos.* **2019**, *54*, 1265–1280. [CrossRef]
3. Yu, D.; Ma, Y.; Wang, S.; Ma, C.; Wei, F. Mineralogy and Preparation of High-Purity Quartz: A Case Study from Pegmatite in the Eastern Sector of the North Qinling Orogenic Belt. *Minerals* **2025**, *15*, 788. [CrossRef]
4. Guo, G.; Bonnetti, C.; Zhang, Z.; Li, G.; Yan, Z.; Wu, J.; Wu, Y.; Liu, X.; Wu, B. SIMS U–Pb Dating of Uraninite from the Guangshigou Uranium Deposit: Constraints on the Paleozoic Pegmatite–Type Uranium Mineralization in North Qinling Orogen, China. *Minerals* **2021**, *11*, 402. [CrossRef]
5. Zhao, H.; Simonetti, A.; Simonetti, S.; Cao, X.; Du, Y. A Geochemical and Isotopic Investigation of Carbonatites from Huangshuian, Central China: Implications for Petrogenesis and Mantle Sources. *Minerals* **2024**, *14*, 953. [CrossRef]
6. Qu, K.; Sima, X.; Li, G.; Fan, G.; Shen, G.; Liu, X.; Xiao, Z.; Guo, H.; Qiu, L.; Wang, Y. Fluorluanshiweiite, $KLiAl_{1.5}\square_{0.5}(Si_{3.5}Al_{0.5})O_{10}F_2$, a New Mineral of the Mica Group from the Nanyangshan LCT Pegmatite Deposit, North Qinling Orogen, China. *Minerals* **2020**, *10*, 93. [CrossRef]
7. Yang, W.; Fang, T.; Wang, Y.; Sha, H. Late Paleozoic Tectonic Evolution of the Qinling Orogenic Belt: Constraints of Detrital Zircon U-Pb Ages from the Southern Margin of North China Block. *Minerals* **2022**, *12*, 864. [CrossRef]
8. Wu, B.; Bonnetti, C.; Liu, Y.; Zhang, Z.-S.; Guo, G.-L.; Li, G.-L.; Hu, Y.-Q.; Yan, Z.-Y. Uraninite from the Guangshigou Pegmatite-Type Uranium Deposit in the North Qinling Orogen, Central China: Its Occurrence, Alteration and Implications for Post-Caledonian Uranium Circulation. *Minerals* **2021**, *11*, 729. [CrossRef]
9. Wang, W.; Tan, S.; Wan, J.; Hu, X.; Peng, H.; Liu, C. Insights from Dikes for Multistage Granitic Magmatism in the Huayangchuan Uranium Polymetallic Deposit, Qinling Orogen. *Minerals* **2024**, *14*, 261. [CrossRef]

10. Du, B.F.; Li, S.P.; Wu, M.Q.; Zhang, R.Z.; Chen, J.K.; Wang, L.; Li, S.S.; Qiu, K.F. Metallogenic age and process of the Shuimogo REE deposit in the south margin of the North China Craton. *Earth Sci. Front.* **2026**, *33*, 247–264. (In Chinese with English abstract)
11. Lei, H.C.; Xia, F.; Ren, Q.; Dang, S.B.; Zhang, H.; Ye, Y.K.; Duan, J.B. Mineralogy, Geochemistry, and geochronology of the Paleoproterozoic pegmatite in the northern margin of the North China Craton, China: Implications for U–Th–Pb–Nb–Ta–REE polymetallic mineralization. *Ore Geol. Rev.* **2025**, *187*, 106948. [CrossRef]
12. Shi, J.P.; Wu, G.; Yang, D.B.; Chen, Y.J.; Yang, H.T. Tectonic extension and pre–enrichment of REEs in the southern margin of the North China Craton during late Paleoproterozoic: Evidence from geochemistry and Lu–Hf–Nd isotopes of Longwangzhuang REE–bearing granite. *Ore Geol. Rev.* **2026**, *191*, 107186. [CrossRef]
13. Li, Z.D.; Li, S.P.; Zeng, W.; Li, X.G.; Pan, X.N.; Zhang, S.B.; Guo, H.; Liu, W.G. Geological, geochemistry and Sr, Nd, Pb isotopic characteristics of the Dazhuang Nb–REE deposit in southern margin of the North China craton. *Acta Geol. Sin.* **2023**, *97*, 82–108. (In Chinese with English abstract)
14. Teng, F.; Zhang, J.; Guo, W.; Bagas, L.; Yan, K.; Teng, Y.; Wei, Y.; Zhou, N.; Gao, Y.; Wei, L. Metamorphic Fluids with Magmatic Overprint in the Huayagou Gold Deposit, West Qinling Orogen, Central China: Evidence from Apatite and Tourmaline in Situ Geochemistry. *Geosciences* **2026**, *16*, 80. [CrossRef]
15. Miao, G.; Dong, G.; Yan, G.; Qi, X.; Xiao, C.; Jiang, H.; Shi, Z. Geochemical Fingerprints of Magnetite in Yechangping Super-Large Mo-W Deposit, Western Henan, China: Constraints on Ore-Forming Evolution and Prospecting Implications. *Minerals* **2026**, *16*, 374. [CrossRef]
16. HIGS (Henan Institute of Geological Survey). *Regional Geology of China: Henan Volume*; Geological Publishing House: Beijing, China, 2024; pp. 1–689. (In Chinese with English abstract)
17. Gao, Q.L.; Zheng, J.P.; Zhang, Z.H.; Xiong, Q.; Chen, X. Complex evolution of the southern margin of the North China Craton: Evidence from LA–ICPMS U–Pb dating of zircons in Zhouzhuang meta–gabbro. *Acta Petrol. Sin.* **2009**, *25*, 3275–3286. (In Chinese with English abstract)
18. Wang, X.L.; Jiang, S.Y.; Dai, B.Z.; Griffin, W.L.; Dai, M.N.; Yang, Y.H. Age, geochemistry and tectonic setting of the Neoproterozoic, ca 830Ma. gabbros on the southern margin of the North China Craton. *Precambrian Res.* **2011**, *190*, 35–47. [CrossRef]
19. Wang, H.; Wu, Y.B.; Qin, Z.W.; Zhu, L.Q.; Liu, Q.; Liu, X.C.; Gao, S.; Wijbrans, J.R.; Zhou, L.; Gong, H.J.; et al. Age and geochemistry of Silurian gabbroic rocks in the Tongbai orogen, central China: Implications for the geodynamic evolution of the North Qinling arc–back–arc system. *Lithos* **2013**, *179*, 1–15. [CrossRef]
20. Wang, H.; Wu, Y.B.; Li, C.R.; Zhao, T.Y.; Qin, Z.W.; Zhu, L.Q.; Gao, S.; Zheng, J.P.; Liu, X.M.; Zhou, L.; et al. Recycling of sediment into the mantle source of K–rich mafic rocks: Sr–Nd–Hf–O isotopic evidence from the Fushui complex in the Qinling orogen. *Contrib. Mineral. Petrol.* **2014**, *168*, 1062. [CrossRef]
21. Li, Z.S.; Jia, C.; Zhao, Z.Y.; Huo, J.J.; Li, Q.Z.; Zhang, J.D. Depositional age and provenance analysis of the Luanchuan Group in the southern margin of North China Craton and its significance for regional tectonic evolution:constraints from zircon U–Pb geochronology and Hf isotopes. *Acta Geol. Sin.* **2020**, *94*, 1046–1066. (In Chinese with English abstract)
22. Peng, P.; Mitchell, R.N.; Zhang, N.; Su, X.; Li, Y.; Sun, F.; Wang, C.; Guo, J.; Zhai, M. Basal mantle structure regenerated through supercontinents. *Nat. Commun.* **2025**, *16*, 9666. [CrossRef]
23. Sun, S.; Dong, Y.; He, D.; Cheng, C.; Liu, X. Thickening and partial melting of the Northern Qinling Orogen, China: Insights from zircon U–Pb geochronology and Hf isotopic composition of migmatites. *J. Geol. Soc.* **2019**, *176*, 1218–1231. [CrossRef]
24. Chang, H.; Hu, P.; Zhou, G.; Zhang, W.; He, Y.; Zhao, Y.; Bauer, A.M.; Hu, Z.; Wu, Y. Development of a back–arc basin from initial rifting to seafloor spreading: Constraints from Paleozoic basic rocks in the North Qinling accretionary orogen, central China. *Geol. Soc. Am. Bull.* **2023**, *136*, 1511–1525. [CrossRef]
25. Zhao, L.; Li, Y.; Xiang, H.; Zheng, J.; Xiao, W.; Chen, X.; Jiang, H.; Xie, Y.; Brouwer, F.M. A Devonian Shoshonitic Appinite–Granite Suite in the North Qinling Orogenic Belt: Implications for Partial Melting of a Water–Fluxed Lithospheric Mantle in an Extensional Setting. *J. Petrol.* **2023**, *64*, egad040. [CrossRef]
26. Liu, X.Y.; Han, X.; Liang, T.; Li, L.M.; Ren, S.L.; Li, J.H. Petrogenesis and tectonic implications of the Fanpu diorite in the northern Qinling orogenic belt. *Chin. J. Geol.* **2024**, *59*, 52–64. (In Chinese with English abstract)
27. Meng, Q.R.; Wu, G.L.; Wan, B.; Zhu, R.X.; Duan, L.; Wang, B.; Hu, J.M. Proto–Tethyan tectonics in East China: A revisit. *Natl. Sci. Rev.* **2025**, *12*, 153. [CrossRef]
28. Zeng, W.; Sun, F.Y.; Li, C.D.; Li, Z.D.; Cheng, Y.H.; Liu, W.G.; Tu, J.R.; Zhang, C.; Liu, X.; Sun, W.Z. Geological and geochemical characteristics of intermediate–basic intrusions in Funiushan area, southern margin of the North China Craton: Implications for tectonic environment and mantle properties in the Early Cretaceous. *Lithos* **2025**, *514–515*, 108193. [CrossRef]
29. Zhang, F.; Li, M.; Dong, Y.; Gan, C.; Zhu, Z.; Han, W.; Wang, Y. Unveiling an Ordovician continental back-arc basin: Insights from the gabbros and adakitic granitoids of the Erlangping unit, Tongbai Orogen (Central China). *Lithos* **2026**, *532–533*, 108506. [CrossRef]
30. Bao, Z.W.; Li, C.J.; Qi, J.P. SHRIMP zircon U–Pb age of the gabbro dyke in the Luanchuan Pb–Zn–Ag orefield, East Qinling orogen and its constraint on mineralization time. *Acta Petrol. Sin.* **2009**, *25*, 2951–2956. (In Chinese with English abstract)

31. Zhao, G.; Wang, Y.; Huang, B.; Dong, Y.; Li, S.; Zhang, G.; Yu, S. Geological reconstructions of the East Asian blocks: From the breakup of Rodinia to the assembly of Pangea. *Earth–Sci. Rev.* **2018**, *186*, 262–286. [CrossRef]
32. Dong, Y.; Santosh, M. Tectonic architecture and multiple orogeny of the Qinling Orogenic Belt, Central China. *Gondwana Res.* **2016**, *29*, 1–40. [CrossRef]
33. Huang, J.H.; Huang, Z.Z.; Chen, D.L.; Li, K.K.; Huang, X.X.; Ren, M.H.; Fan, Y.Z. Tectonic Setting of the Neoproterozoic Gabbroic Intrusions in the Luanchuan Area, Southern Margin of the North China Craton: Constraints from Ilmenite and Biotite Mineralogy. *Minerals* **2025**, *15*, 602. [CrossRef]
34. Zhao, L.G.; Li, C.D.; Xu, Y.W.; Wu, Z.Y.; Chang, Q.S.; Xu, T.; Teng, X.M. Geochemistry of Nb–Enriched Gabbros in Zhaigen Area in Northern Qinling and Their Tectonic Significance. *Earth Sci.* **2019**, *44*, 135–144. (In Chinese with English abstract)
35. Chen, Y.; Zhou, Z.; Xu, C. Transition from orogenic plateau to thinning reveals mesozoic North China craton dynamics. *Commun. Earth Environ.* **2025**, *6*, 791. [CrossRef]
36. Ren, L.; Liang, H.; Bao, Z.; Huang, W. Early Paleozoic magmatic "flare–ups" in western Qinling orogeny, China: New insights into the convergence history of the North and South China Blocks at the northern margin of Gondwana. *Lithos* **2021**, *380–381*, 105833. [CrossRef]
37. Zhao, T.P.; Zhou, M.F.; Zhai, M.; Xia, B. Paleoproterozoic Rift–Related Volcanism of the Xiong'er Group, North China Craton: Implications for the Breakup of Columbia. *Int. Geol. Rev.* **2002**, *44*, 336–351. [CrossRef]
38. Hu, G.H.; Zhang, S.H.; Zhang, Q.Q.; Wang, S.Y. New geochronological constraints on the Dahongkou Formation of the Luanchuan Group and its implications on the Neoproterozoic tectonic evolution of the southern margin of the North China Craton. *Acta Petrol. Sin.* **2019**, *35*, 2503–2517. (In Chinese with English abstract)
39. Li, Y.; Yang, J.; Dilek, Y.; Zhang, J.; Pei, X.; Chen, S.; Xu, X.; Li, J. Crustal architecture of the Shangdan suture zone in the early Paleozoic Qinling orogenic belt, China: Record of subduction initiation and backarc basin development. *Gondwana Res.* **2015**, *27*, 733–744. [CrossRef]
40. Pang, L.Y.; Zhu, X.Y.; Hu, G.H.; Qiu, Y.F.; Su, W.B.; Wang, S.Y.; Zhao, T.P. Advances in the study of Meso–Neoproterozoic stratigraphic chronology and sedimentary evolution in the southern margin of the North China Craton. *J. Stratigr.* **2021**, *45*, 180–195. (In Chinese with English abstract)
41. Zeng, L.; Zheng, H.; Zhang, D.; Han, S.; Peng, H.; Kang, P.; Ma, S. Early Palaeozoic PTtD paths of the eastern Shangdan Shear Zone in Qinling Orogen, central China. *Int. Geol. Rev.* **2025**, *23*, 2495–2520. [CrossRef]
42. Diwu, C.; Long, X.; Li, S. Tectonic evolution of the North Qinling Orogenic Belt, Central China: Insights from metamafic rocks of the Songshugou Complex. *Geol. J.* **2018**, *54*, 2382–2399. [CrossRef]
43. Wiedenbeck, M.; AllÉ, P.; Corfu, F.; Griffin, W.L.; Meier, M.; Oberli, F.; Quadt, A.V.; Roddick, J.C.; Spiegel, W. Three Natural Zircon Standards for U–Th–Pb, Lu–Hf, Trace Element and Ree Analyses. *Geostand. Newsl.* **1995**, *19*, 1–23. [CrossRef]
44. Sláma, J.; Košler, J.; Condon, D.J.; Crowley, J.L.; Gerdes, A.; Hanchar, J.M.; Horstwood, M.S.A.; Morris, G.A.; Nasdala, L.; Norberg, N.; et al. Plešovice zircon—A new natural reference material for U–Pb and Hf isotopic microanalysis. *Chem. Geol.* **2008**, *249*, 1–35. [CrossRef]
45. Andersen, T. Correction of common lead in U–Pb analyses that do not report 204Pb. *Chem. Geol.* **2002**, *192*, 59–79. [CrossRef]
46. Vermeesch, P. IsoplotR: A free and open toolbox for geochronology. *Geosci. Front.* **2018**, *9*, 1479–1493. [CrossRef]
47. Sun, S.S.; McDonough, W.F. Chemical and isotopic systematics of oceanic basalts: Implications for mantle composition and processes. *Geol. Soc. Lond. Spec. Publ.* **1989**, *42*, 313–345. [CrossRef]
48. Rubatto, D.; Gebauer, D. Use of cathodoluminescence for U–Pb zircon dating by IOM Microprobe: Some examples from the western Alps. In *Cathodoluminescence in Geosciences*; Pagel, M., Barbin, V., Blanc, P., Ohnenstetter, D., Eds.; Springer: Berlin/Heidelberg, Germany, 2000; pp. 373–400.
49. Wu, Y.B.; Zheng, Y.F. Genesis of zircon and its constraints on interpretation of U–Pb age. *Chin. Sci. Bull.* **2004**, *49*, 1554–1569. [CrossRef]
50. Siebel, W.; Schmitt, A.K.; Danišík, M.; Chen, F.; Meier, S.; Weiß, S.; Eroğlu, S. Prolonged mantle residence of zircon xenocrysts from the western Eger rift. *Nat. Geosci.* **2009**, *2*, 886–890. [CrossRef]
51. Hoskin, P.W.O.; Ireland, T.R. Rare earth element chemistry of zircon and its use as a provenance indicator. *Geology* **2000**, *28*, 627–630. [CrossRef]
52. Hoskin, P.W.O.; Schaltegger, U. The Composition of Zircon and Igneous and Metamorphic Petrogenesis. *Rev. Mineral. Geochem.* **2003**, *53*, 27–62. [CrossRef]
53. Middlemost, E.A. Naming materials in the magma/igneous rock system. *Earth–Sci. Rev.* **1994**, *37*, 215–224. [CrossRef]
54. De la Roche, H.D.; Leterrier, J.T.; Grandclaude, P.; Marchal, M. A classification of volcanic and plutonic rocks using R1 R2–diagram and major–element analyses—Its relationships with current nomenclature. *Chem. Geol.* **1980**, *29*, 183–210. [CrossRef]
55. Miyashiro, A. Classification, Characteristics, and Origin of Ophiolites. *J. Geol.* **1975**, *83*, 249–281. [CrossRef]
56. Irvine, T.N.; Baragar, W.R.A. A Guide to the Chemical Classification of the Common Volcanic Rocks. *Can. J. Earth Sci.* **1971**, *8*, 523–548. [CrossRef]

57. Pearce, J.A. Trace element characteristics of lavas from destructive plate boundaries. In *Andesites: Orogenic Andesites and Related Rocks*; Thorpe, R.S., Ed.; John Wiley and Sons: Hoboken, NJ, USA, 1982; pp. 528–548.
58. Gillis, K.M.; Banerjee, N.R. Hydrothermal alteration patterns in supra–subduction zone ophiolites. In *Ophiolites and Oceanic Crust: New Insights from Field Studies and the Ocean Drilling Program*; Geological Society of America: Boulder, CO, USA, 2000; Volume 349, pp. 283–297.
59. Winchester, J.A.; Floyd, P.A. Geochemical magma type discrimination: Application to altered and metamorphosed basic igneous rocks. *Earth Planet. Sci. Lett.* **1976**, *28*, 459–469. [CrossRef]
60. Polat, A.; Hofmann, A.W.; Rosing, M.T. Boninite–like volcanic rocks in the 3.7–3.8 Ga Isua greenstone belt, West Greenland: Geochemical evidence for intra–oceanic subduction zone processes in the early Earth. *Chem. Geol.* **2002**, *184*, 231–254. [CrossRef]
61. Polat, A.; Hofmann, A.W. Alteration and geochemical patterns in the 3.7–3.8 Ga Isua greenstone belt, West Greenland. *Precambrian Res.* **2003**, *126*, 197–218. [CrossRef]
62. Castro, A. The Appinite–Migmatite Complex of Sanabria, NW Iberian Massif, Spain. *J. Petrol.* **2003**, *44*, 1309–1344. [CrossRef]
63. Rudnick, R.L.; Gao, S. Composition of the Continental Crust. *Treatise Geochem.* **2003**, *3*, 1–64.
64. Wilson, M.E. *Igneous petrogenesis: A Global Tectonic Approach*; Springer: Dordrecht, The Netherlands; London, UK, 1989; pp. 1–466.
65. Workman, R.K.; Hart, S.R. Major and trace element composition of the depleted MORB mantle, DMM. *Earth Planet. Sci. Lett.* **2005**, *231*, 53–72. [CrossRef]
66. Dai, L.Q.; Zhao, Z.F.; Zheng, Y.F. Tectonic development from oceanic subduction to continental collision: Geochemical evidence from postcollisional mafic rocks in the Hong'an–Dabie orogens. *Gondwana Res.* **2015**, *27*, 1236–1254. [CrossRef]
67. Geng, H.; Sun, M.; Yuan, C.; Zhao, G.; Xiao, W. Geochemical and geochronological study of early Carboniferous volcanic rocks from the West Junggar: Petrogenesis and tectonic implications. *J. Asian Earth Sci.* **2011**, *42*, 854–866. [CrossRef]
68. Scandolara, J.E.; Ribeiro, P.S.E.; Frasca, A.A.S.; Fuck, R.A.; Rodrigues, J.B. Geochemistry and geochronology of mafic rocks from the Vespor suite in the Juruena arc, Roosevelt–Juruena terrain, Brazil: Implications for Proterozoic crustal growth and geodynamic setting of the SW Amazonian craton. *J. S. Am. Earth Sci.* **2014**, *53*, 20–49. [CrossRef]
69. Khalil, A.E.S.; Obeid, M.A.; Azer, M.K. Late Neoproterozoic post–collisional mafic magmatism in the Arabian–Nubian Shield: A case study from Wadi El–Mahash gabbroic intrusion in southeast Sinai, Egypt. *J. Afr. Earth Sci.* **2015**, *105*, 29–46. [CrossRef]
70. Kara, J.; Leskelä, T.; Väisänen, M.; Skyttä, P.; Lahaye, Y.; Tiainen, M.; Leväniemi, H. Early Svecofennian rift–related magmatism: Geochemistry, U–Pb–Hf zircon isotope data and tectonic setting of the Au–hosting Uunimäki gabbro, SW Finland. *Precambrian Res.* **2021**, *364*, 106364. [CrossRef]
71. Wang, K.; Plank, T.; Walker, J.D.; Smith, E.I. A mantle melting profile across the Basin and Range, SW USA. *J. Geophys. Res. Solid Earth* **2002**, *107*, 5–21. [CrossRef]
72. Aldanmaz, E.; Pearce, J.A.; Thirlwall, M.F.; Mitchell, J.G. Petrogenetic evolution of late Cenozoic, post–collision volcanism in western Anatolia, Turkey. *J. Volcanol. Geotherm. Res.* **2000**, *102*, 67–95. [CrossRef]
73. Sandeman, H.; Hanmer, S.; Tella, S.; Armitage, A.; Davis, W.; Ryan, J. Petrogenesis of Neoarchaean volcanic rocks of the MacQuoid supracrustal belt: A back–arc setting for the northwestern Hearne subdomain, western Churchill Province, Canada. *Precambrian Res.* **2006**, *144*, 140–165. [CrossRef]
74. Salters, V.J.M.; Stracke, A. Composition of the depleted mantle. *Geochem. Geophys. Geosystems* **2004**, *5*, Q05B07. [CrossRef]
75. McKenzie, D.A.N.; O'Nions, R.K. Partial melt distributions from inversion of rare earth element concentrations. *J. Petrol.* **1991**, *32*, 1021–1091. [CrossRef]
76. Zheng, F.; Dai, L.Q.; Zhao, Z.F.; Zheng, Y.F.; Xu, Z. Recycling of Paleo–oceanic crust: Geochemical evidence from Early Paleozoic mafic igneous rocks in the Tongbai orogen, Central China. *Lithos* **2019**, *329*, 312–327. [CrossRef]
77. Shaw, D.M. Trace element fractionation during anatexis. *Geochim. Cosmochim. Acta* **1970**, *34*, 237–243. [CrossRef]
78. Kinzler, R.J. Melting of mantle peridotite at pressures approaching the spinel to garnet transition: Application to mid-ocean ridge basalt petrogenesis. *J. Geophys. Res. Solid Earth* **1997**, *102*, 853–874. [CrossRef]
79. Walter, M.J. Melting of Garnet Peridotite and the Origin of Komatiite and Depleted Lithosphere. *J. Petrol.* **1998**, *39*, 29–60. [CrossRef]
80. Pearce, J.A.; Cann, J.R. Tectonic setting of basic volcanic rocks determined using trace element analyses. *Earth Planet. Sci. Lett.* **1973**, *19*, 290–300. [CrossRef]
81. Meschede, M. A method of discriminating between different types of mid–ocean ridge basalts and continental tholeiites with the Nb–Zr–Y diagram. *Chem. Geol.* **1986**, *56*, 207–218. [CrossRef]
82. Agrawal, S.; Guevara, M.; Verma, S.P. Tectonic Discrimination of Basic and Ultrabasic Volcanic Rocks through Log–Transformed Ratios of Immobile Trace Elements. *Int. Geol. Rev.* **2010**, *50*, 1057–1079. [CrossRef]
83. Boedo, F.L.; Vujovich, G.I.; Kay, S.M.; Ariza, J.P.; Pérez Luján, S.B. The E–MORB like geochemical features of the Early Paleozoic mafic–ultramafic belt of the Cuyania terrane, western Argentina. *J. S. Am. Earth Sci.* **2013**, *48*, 73–84. [CrossRef]
84. Bonin, B. Do coeval mafic and felsic magmas in post–collisional to within–plate regimes necessarily imply two contrasting, mantle and crustal, sources? A review. *Lithos* **2004**, *78*, 1–24. [CrossRef]

85. Wang, W.; Pandit, M.K.; Zhao, J.H.; Chen, W.T.; Zheng, J.P. Slab break–off triggered lithosphere–asthenosphere interaction at a convergent margin: The Neoproterozoic bimodal magmatism in NW India. *Lithos* **2018**, *299*, 281–296. [CrossRef]
86. Yu, H.; Zhang, H.F.; Li, X.H.; Zhang, J.; Santosh, M.; Yang, Y.H.; Zhou, D.W. Tectonic evolution of the North Qinling Orogen from subduction to collision and exhumation: Evidence from zircons in metamorphic rocks of the Qinling Group. *Gondwana Res.* **2016**, *30*, 65–78. [CrossRef]
87. Liang, L.; Li, W.; Dong, Y.; Zhang, L.; Sheir, F.; Jiang, L.; Feng, Z.; Wang, C.; Basil, A.; Ma, Z. Late Palaeozoic tectonic transformation of the North Qinling Orogenic Belt: Insight from the geochronology, geochemistry and Sr-Nd-Hf isotopes of Carboniferous magmatic rocks. *Geol. J.* **2024**, *59*, 1280–1297. [CrossRef]
88. Torsvik, T.H.; Cocks, L.R.M. Gondwana from top to base in space and time. *Gondwana Res.* **2013**, *24*, 999–1030. [CrossRef]
89. Bader, T.; Zhang, L.; Li, X. Is the Songshugou Complex, Qinling Belt, China, an Eclogite Facies Neoproterozoic Ophiolite? *J. Earth Sci.* **2019**, *30*, 460–475. [CrossRef]
90. Li, H.; Yan, K.; Li, K.; Yang, K.; Fan, B.; Xue, Z.; Chen, L.; Guo, H. Detrital Zircon U–Pb Age Data and Geochemistry of Clastic Rocks in the Xiahe–Hezuo Area: Implications for the Late Paleozoic–Mesozoic Tectonic Evolution of the West Qinling Orogen. *Geosciences* **2025**, *15*, 384. [CrossRef]
91. Yuan, F.; Jiang, S.Y.; Liu, J.; Zhang, S.; Xiao, Z.; Liu, G.; Hu, X. Geochronology and Geochemistry of Uraninite and Coffinite: Insights into Ore-Forming Process in the Pegmatite-Hosted Uraniferous Province, North Qinling, Central China. *Minerals* **2019**, *9*, 552. [CrossRef]
92. Zhang, H.F.; Zhang, B.R.; Harris, N.; Zhang, L.; Chen, Y.L.; Chen, N.S.; Zhao, Z.D. U–Pb zircon SHRIMP ages, geochemical and Sr–Nd–Pb isotopic compositions of intrusive rocks from the Longshan–Tianshui area in the southeast corner of the Qilian orogenic belt, China: Constraints on petrogenesis and tectonic affinity. *J. Asian Earth Sci.* **2006**, *27*, 751–764. [CrossRef]
93. Qin, J.F.; Lai, S.C.; Long, X.P.; Zhang, Z.Z.; Ju, Y.J.; Zhu, R.Z.; Wang, X.Y.; Li, Y.F.; Wang, J.B.; Li, T. Thermotectonic evolution of the Paleozoic granites along the Shangdan suture zone, central China): Crustal growth and differentiation by magma underplating in an orogenic belt. *GSA Bull.* **2021**, *133*, 523–538. [CrossRef]
94. Mao, X.H.; Zhang, J.X.; Yu, S.Y.; Li, Y.S.; Yu, X.X.; Lu, Z.L. Early Paleozoic granulite–facies metamorphism and anatexis in the northern West Qinling orogen: Monazite and zircon U–Pb geochronological constraints. *Sci. China Earth Sci.* **2017**, *60*, 943–957. [CrossRef]
95. Vanderhaeghe, O.; Teyssier, C. Crustal–scale rheological transitions during late–orogenic collapse. *Tectonophysics* **2001**, *335*, 211–228. [CrossRef]

Disclaimer/Publisher's Note: The statements, opinions and data contained in all publications are solely those of the individual author(s) and contributor(s) and not of MDPI and/or the editor(s). MDPI and/or the editor(s) disclaim responsibility for any injury to people or property resulting from any ideas, methods, instructions or products referred to in the content.